United Nations Educational, Scientific and Cultural Organization
Geothermal Training Programme Under the auspices of UNESCO

GRÓ GTP, Grensásvegur 9,
IS-108 Reykjavík, Iceland

Reports 2021
Number 24

PROCESSING AND 1D JOINT INVERSION OF MT AND TEM RESISTIVITY DATA FROM BURANGA GEOTHERMAL FIELD, UGANDA

Fred Ssemuyaba
Ministry of Energy and Mineral Development
Geothermal Resources Department
P.O. Box 9, Entebbe
UGANDA
fredwilkins2@gmail.com, frss@grogtp.is

ABSTRACT

Buranga geothermal prospect is the most promising geothermal area in the western branch of the East African Rift System (EARS). Buranga is located at the north-western base of the Rwenzori mountains and approximately 50 km southwest of Fort portal town in Uganda. It is a deep circulation amagmatic system controlled by NE SW trending deep-seated faults of the Albertine graben which form a border between the Buranga (Semliki) flood plain and the Rwenzori massif. This report highlights the key findings of the 1D joint inversion of Magnetotellurics (MT) and Time Domain Electromagnetics (TDEM) data from the area. Resistivity inversion results indicate that the geoelectric strike is in NE SW direction parallel to the major bounding Bwamba fault. Results from this joint inversion indicate a low resistivity in the sediments due to salinity of the geothermal fluids (14,000 -17,000 mg/kg and/or geothermal alteration in the middle of the prospect at the border of the sedimentary basin and the Rwenzori massif. This conductive zone extends to a depth close to 5 km b.s.l, which is close to the depth to the basement that has been estimated at 5000 m b.s.l by oil and gas exploration drilling within the vicinity of the prospect.

1. INTRODUCTION

Over the recent past, the Ministry of Energy and Mineral Development of Uganda, through the Geothermal Resources Department (GRD), has embarked on the search for alternative energy sources in response to the ever-increasing demand for clean, renewable and sustainable energy resources to support the growing economy in the different sectors, such as of agriculture, extractive industries, manufacturing industries, tourism and other small scale value addition chains. One of the energy resources that has been earmarked for exploitation is geothermal energy.

Geothermal prospects in Uganda are located in the western branch of the East African rift system (EARS) in the Albertine Graben and thus are mostly fault-controlled, deep amagmatic systems (Kahwa et al., 2020). This makes these areas somewhat special compared to conventional high temperature volcanic-hosted geothermal fields that are found in the Eastern branch of the East African rift system and other parts of the world. Owing to the uniqueness of the prospects in Uganda, GRD has adapted a site-specific approach of exploration focusing on acquiring geoscientific data and integrating the results

in conceptual models directed at targeting geothermal reservoirs heated to up to 180°C by deep circulation, like those typical of the United States Basin and Range as well as Western Turkey (Heath et al., 2018). This site-specific exploration approach is aimed at reducing the upfront geologic risks associated with drilling in deep circulation fault-controlled systems that might arise if proper geoscientific data integration is not undertaken.

Therefore, in addition to structural geological mapping campaigns and geochemical surveys, Magnetotelluric (MT) and Transient Electromagnetic (TEM) resistivity surveys have been carried out at Buranga (also referred to as Sempaya) to help investigate the characteristics of the resistivity structure in the area to allow for proper delineation of exploitable geothermal reservoir as well as establishing the potential resource size. In addition, resistivity surveys at Buranga were intended to identify fault offset of low resistivity sediments and high resistivity Precambrian rocks and detect low resistivity clay caps over potential high resistivity aquifers in the sediments. The MT method has successfully been used to detect and characterise geothermal areas located in similar extensional tectonics where faults and fractures play a significant role in the deep circulation of geothermal fluids and heat transfer from deep to shallow crustal levels (Faulds et al., 2009; Kahwa et al., 2020).

This report focuses on the processing and 1D joint inversion of MT and TEM data collected at Buranga and integrating the results with other geologic information to help decision making on whether to drill, and if so, where to drill test holes (temperature gradient holes) which is less expensive compared to conventional deep exploration drilling.

2. LOCATION AND GEOLOGY OF BURANGA

2.1 Location

The Buranga geothermal field is located within the Albertine graben that forms a part of the western branch of the East African Rift System (Figure 1) that runs along the joint border of Uganda and the Democratic Republic of Congo (DRC). The Buranga geothermal field is located in the Kasitu sub-county in Bwamba county of Bundibugyo district (Nyaketcho., 2008, Sempaya geologic map sheet 56/1). It is located 50 km southwest of Fort Portal town in Bundibugyo district which lies in Western Uganda. It is bordered by the Ntoroko district in the northeast, Kabarole in the east and southeast and by the Democratic Republic of Congo in the west.

This prospect area is located in the Semliki Kaiso sedimentary basin some 300 to 600 m northwest of the Bwamba escarpment which forms the NW boundary of the Rwenzori Massif. It lies under the Bwamba fault which strikes 20-40° to the northeast and has a dip of 60-65° to the west. The sedimentary basin around Buranga is generally covered with boulder beds and scree but the geothermal activity is found in an area of swamps and rain forest. Surface manifestations cover an area of about 0.12 km^2 and consist of three main hot spring areas: The Mumbuga springs, the Nyansimbe pool and the Kagoro springs. These three groups of springs lay approximately on a line extending some 550 m along a N-35°-E strike, approximately parallel to the Bwamba fault. In addition to these three hot spring groups, springs are found in an area extending some 350 m SE of the Nyansimbe pool.

2.2 Regional and local geology

Uganda is made up of an exposed Precambrian basement dissected by the western branch of the East African Rift System in the western part of the country. The Western branch, the Albertine Rift, starts in the north at the Sudan border, curves to the west and then southwest along the border with the Democratic Republic of Congo, and then runs south to Rwanda, Burundi, and western Tanzania (Figure 1). Spreading in the EARS began at least 15 million years ago in Miocene time. The western rift is

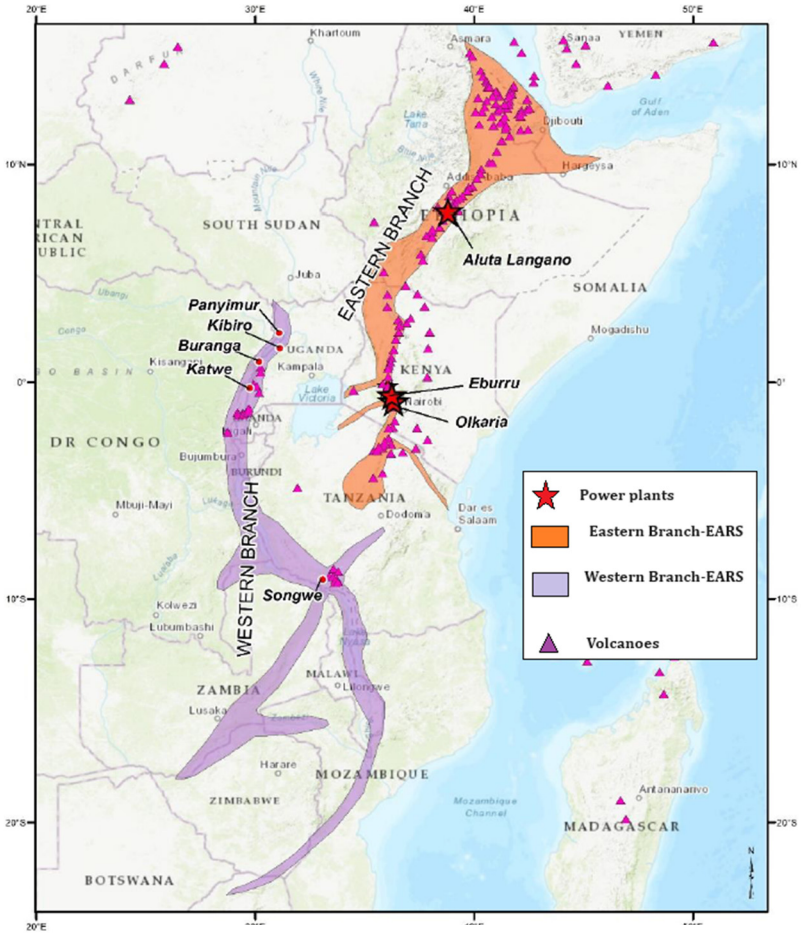

FIGURE 1: Map of the EARS. The purple colour highlights the Western branch while the orange colour highlights the Eastern branch. Volcano data is extracted from the Smithsonian global database (Modified from Hinz et al., 2016)

considered to be younger (late Miocene-Recent) than the more mature eastern branch (Morley and Westcott, 1999). The Albertine rift is seismically active, characterized by deep (27- 40 km), large earthquakes (Lindenfeld et al., 2012). The region of the rift has a markedly higher heat flow than the surrounding Precambrian terrain (Natukunda.,2010). Two different echelon strands are found in the Western Rift Valley, separated by the Rwenzori Mountains, which rise from a base of less than 1,000 m.a.s.l in the rift to over 5,000 m.a.s.l. in the rift valley. There are thick layers of late Tertiary and Quaternary sediments, freshwater, and saline crater lakes. Volcanic and plutonic bodies have been identified beneath L. Albert and L. Edward in the south (EDICON, 1984; Natukunda, 2010).

Buranga geothermal area is located at the north-western base of the Rwenzori Mountains in the Western rift valley. A tertiary succession of sands, clays and boulder beds with occasional tuffs has been identified in exploration drilling data. Geological logs from old boreholes at Buranga indicate that the Tertiary succession is terminated in the main Bwamba fault zone by a breccia cemented by calc tuff followed by mylonite (Harris et al., 1956; Natukunda., 2010). In addition, according to Natukunda (2010), the clays are of various colours and the sands are fine-to medium-grained, varying in colour between white, brown, grey, and green. The most common binding material is clay, although this is patchily replaced by calcium carbonate, giving rise to calcareous sandstones and grits.

2.2.1 Structural geology and fault dip measurements

Measured dips on exposed fault surfaces in Precambrian rock east of the hot springs range from 50-60°, average 55° to NW which is similar to the 64° calculated based on the intercepts in Borehole 1 (McConnel and Brown.,1954). Striations indicate dip-slip motion and a WNW-ESE extension direction.

During a post field presentation in 2017, the East Africa Geothermal Energy Facility (EAGER) team described the faults surrounding the Rwenzori block and through the prospect area as being Quaternary active structures with the footwall and hanging wall faults being associated with the Quaternary fault scarp. The area is highly vegetated, so smaller Quaternary fault scarps and fault splays are probably not recognised.

2.3 Previous exploration activities

According to Kato (2017), the earliest geothermal exploration activities in Uganda date as far back as the early 1950s, however, the first detailed exploration phase was undertaken as a collaboration between the Government of Uganda (GoU), the Organisation of Petroleum Exporting Countries (OPEC), the Government of Iceland through ICEIDA (The Icelandic International Development Agency) and the United Nations Development Programme (UNDP) from 1993 to 1994 where three (3) highly ranking prospects, i.e, Katwe, Buranga, and Kibiro, were investigated. The major activities included geological, geochemical, and isotope surveys.

From 1999 to 2003, the International Atomic Energy Agency (IAEA) together with the Ministry of Energy and Mineral Development (MEMD) funded a project called "The Isotope hydrology for exploring geothermal resources phase 1" with the aim of upgrading and refining the exploration models of Kibiro, Buranga and Katwe-Kikrongo prospects, using isotopes. This was a follow up of the UNDP-ICEIDA project of 1992-1994.

The German Federal Institute for Geosciences and Natural Resources (BGR) together with MEMD conducted intermediate exploration in Buranga beginning in 2003. This was part of the GEOTHERM programme which promoted the utilization of geothermal energy in developing countries. Project activities included surface water sampling and analysis, isotopic studies, geophysical surveys (gravity, TEM, and Schlumberger resistivity soundings). A micro-earthquake survey was conducted around Buranga to map seismically active structures (Ochmann et al., 2007; Kato, 2017). Results indicated active Rwenzori bounding faults, presumed to control geothermal fluid flow. A magma body was inferred under Rwenzori Mountain. Elevated 3He/4He ratios in geothermal fluids from the isotopic and water sampling surveys were believed to be evidence of deep permeability and possibly deeper, higher-temperature fluid reservoirs.

In 2015, M/s GIDDS, a private exploration licence holder at Buranga, acquired data from 32 MT stations and 38 TEM stations using the expertise of geophysicists from GDC in Kenya. More detailed and infill surveys had been recommended at that time in the preliminary data analysis report that was submitted by the licence holder to GRD as part of his quarterly activity report.

In 2011, the Uganda Geothermal Resources Development Project 1199 (UGRDP), which was fully funded by the Government of Uganda (GoU), came on board to undertake appraisal studies on all the geothermal prospects of the country and to rank these areas according to their priority. During this project a total of 23 geothermal areas were appraised; Kibiro, Buranga and Panyimur geothermal prospects were ranked highest. At Buranga, detailed structural geological mapping, geochemical surveys, soil temperature surveys and geophysical surveys were conducted between 2015 and 2019. This report focuses on the processing and interpretation of the MT and TEM resistivity data that were collected in Buranga during this period with the aim to study the resistivity structure of the area as well comparing it with other geoscientific data from the area.

3. GEOTHERMAL EXPLORATION METHODS

The goal of geothermal exploration is to facilitate the extraction of hot fluids from depth for power production or direct use. This is done by a series of scientific-based work processes for detecting and delineating exploitable geothermal resources, understanding their characteristics, constructing a working/viable preliminary model of the area coupled with an initial resource estimate/assessment to guide the siting of wells. Due to the complexity of the subsurface systems, effective exploration methods are crucial for successful geothermal development. The complexity of geothermal subsurface systems, therefore, necessitates a multidisciplinary approach where geology, geochemistry, geophysics, and other geoscientific techniques complement each other.

3.1 Structural and geological mapping

In a geothermal "green-field", geological mapping is the first step of exploration obtaining crucial information about the surface features of the area. In geological surveys, geothermal manifestations are mapped as well as the surface distribution and type of rocks, and geological structures such as faults, fractures and joints which might be conduits for fluid migration from the subsurface. Although this method is limited to mainly surface observations which might not give very precise subsurface conditions, reservoir physical parameters and arrangement, it is usually of immense importance when used jointly with geoscientific data to help understanding the intricate nature of the subsurface.

The deliverables from a typical geological mapping campaign are usually maps, cross-sections, and sometimes an initial geological conceptual model of the area. The model usually indicates the up-flow and outflow zones, the heat source and estimated depth to the reservoir, main controlling structures such as fractures and faults as well as the lithologic units. Geological conceptual models are very preliminary when it comes to subsurface conditions but they provide vital surface information that is used for later integrated conceptual modelling of the area.

3.2 Geochemical surveys

Geochemical surveys are usually undertaken to study the chemical composition of the fluids at the surface and estimate the interactions and chemical processes that have taken place at depth. Therefore, in the presence of hot spring fluids and fluids from fumaroles, geochemical methods are used to estimate the reservoir temperature using chemical, gas, and water geothermometers. Geochemistry plays a crucial role in informing us about reservoir properties such as salinity, fluid equilibrium state, fluid origin, fluid flow directions, source of recharge, etc. Geological mapping helps to shed light on the expected temperatures at the site, based mainly on temperature measurements from surface geothermal manifestations such as hot springs, geysers, and mud pools. It can also provide insight into the extent of the field as well as choosing drilling targets based on the integration of data from remote sensing, structural mapping, and soil temperature surveys.

3.3 Soil temperature surveys

A soil temperature survey is often deployed together with gas flux measurements during the initial stages of geothermal exploration. It involves the collection of surface temperature data by using thermistor rods pushed about 50 cm into the soil and then measuring the temperature at those depths. Soil gas flux on the other hand measures the up flow of gases, usually CO_2, H_2S and Radon, in areas with notable fractures. These methods are useful in delineating areas of elevated heat and mass transfer in areas with wide fracture zones and faults. However, in blind and heavily capped geothermal areas, soil gas flux and shallow temperature measurements can be rather misleading.

3.4 Geophysical methods

Geological and geochemical mapping is usually limited to direct observations on the surface and limited conclusions and extrapolation that can be drawn about the system and possible underlying structures. Geophysical surface exploration methods measure the surface signatures of properties and processes at depth. Geophysical exploration methods can be classified into several groups such as seismic methods, electrical resistivity methods, potential methods (gravity and magnetics), heat flow measurements, and surface deformation measurements.

Regarding geothermal exploration, geophysical methods are classified into those that are directly related to the parameters that are diagnostic to and characterize the reservoir (direct methods) and those that are indirectly related to the reservoir, known as the structural or indirect methods. During the exploration stage, geophysical surveys are meant to help outline the size of the area (extent), locate the geothermal reservoir, estimate the depth to the reservoir, estimate reservoir parameters such as permeability, location of the clay cap and also the nature of reservoir rocks and finally help to site wells.

Additionally, there are geophysical methods used to monitor reservoir behaviour when geothermal fields are under development or production. Microgravity, ground/surface deformation and micro-seismicity techniques provide indispensable information on reservoir behaviour (such as fault-related permeability from hypocentre distribution analysis or simple shear dilation – permeability enhancement relationships), consequently enabling the development of better production and reinjection strategies to improve sustainable utilisation (e.g. Bromley, 2018).

3.4.1 Indirect (structural) methods

These methods focus on detecting geological formations or structures. These methods include:

- Gravity surveys: They delineate features such as faults, dense intrusions, or sediments on a dense basement; and
- Magnetic surveys: These can trace narrow linear (magnetised) features like dykes and faults where the basement is covered with soil (or dense vegetation in tropical countries). Correlation has often been noticed between low magnetization and zones of intense hydrothermal alteration.

3.4.2 Direct methods

Here the variations in the physical properties are more directly related to the geothermal resource. Examples are:

- Resistivity surveys: Resistivity is dependent on key parameters, such as pore structure, water saturation, salinity, temperature and alteration minerals, characterising a geothermal system; and
- Temperature measurements: These are used to determine the temperature gradient and the total heat flow in an area. They are usually done in shallow holes or temperature gradient holes and exploration wells.

Quantitative results are obtained when thermal gradients are converted to heat flow through the use of Fourier´s equation (Manzella., 2007; Kahwa., 2012):

$$\frac{\Delta T}{\Delta Z} = \frac{\Phi z}{K} \quad (1)$$

where $\Delta T/\Delta Z$ = Vertical temperature gradient (°C m^{-1});
Φz = Conductive heat flow density (W/m^2); and
K = Thermal conductivity (W/m°C).

4. METHODOLOGY

4.1 Choice of methods

In this study, emphasis has been put on the resistivity methods because they are commonly found to be the most powerful geophysical methods in geothermal exploration due to their capability to

measure/detect resistivity anomalies in the subsurface. Resistivity is related to key geothermal parameters such as pore structure, water saturation, salinity, alteration minerals, and temperature.

4.1.1 Fundamentals of resistivity methods

Resistivity methods in geothermal exploration have been discussed by several researchers and scholars. The fundamentals discussed here are mainly based on the publications by Hersir et al. (2021) and Hersir and Árnason (2013).

4.1.2 Resistivity of rocks

From Ohm´s law, the electrical field **E** (V/m) at a particular point in a material is proportional to the current density $\boldsymbol{j}$ (A/m^2):

$$\boldsymbol{E} = \rho \boldsymbol{j} \tag{2}$$

The proportionality constant ρ depends on the type of material and is called the (specific) resistivity whose unit is Ωm. The reciprocal of the resistivity is the conductivity. Electrical conduction in materials takes place by the movement of electrons and ions. Conductivity in rocks is mostly through pore fluid conduction and surface conduction due to adsorbed ions at the rock/water interface (Figure 2). Mineral conduction is negligible in most cases since the rock matrix is normally an insulator.

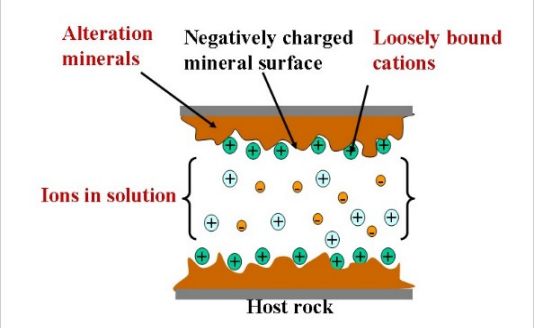

FIGURE 2: Conduction mechanisms in rocks (Hersir et al., 2021)

The resistivity of rocks is influenced by many factors with the most important factors being:

(a) Porosity and pore structure of the rock

The porosity of a material is defined as the ratio of the pore volume to the total volume of the rock

$$\varphi_t = \frac{V_\varphi}{V} \tag{3}$$

Where, φ_t = Fractional porosity;
V_φ = Volume of pores; and
V = Total volume of the rock.

The degree of saturation and porosity are of great importance for the bulk resistivity of the rock. If the pore fluid is more conductive than the rock matrix, Archies law approximates the relation between pore fluid resistivity and porosity as:

$$\rho = \frac{\rho_w\, a}{\emptyset_t^n} \tag{4}$$

Where $\emptyset_t$ = Porosity in proportions of total volume (0-1);
ρ_w = Resistivity of the pore fluid (Ωm);
ρ = Bulk resistivity (Ωm);
a = Parameter describing porosity ≅ 1; and
n = Cementation factor ≅ 2.

(b) The temperature of pore fluids

At moderate temperatures (0 – 200°C), an increase in temperature causes decrease in resistivity of aqueous solutions due to the increase of mobility of ions caused by a reduction in viscosity of the water. This relationship has been described by Dakhnov (1962) by the relation:

$$\rho_w = \frac{\rho_{wo}}{1+\alpha(T-T_0)} \quad (5)$$

Where ρ_{wo} = Resistivity of fluid at reference temperature T_o;
ρ_w = Resistivity of the fluid at temperature T (Ωm);
α = Temperature coefficient of resistivity (°C) α ≅ 0.023 $°C^{-1}$ for T_o = 25°C;
T = Temperature (°C); and
T_o = Reference temperature.

However, at temperatures exceeding 300°C, increasing temperature increases the resistivity of the fluid due to the decrease in the dielectric permittivity of water resulting in a decrease in the number of dissociated ions in the solution.

(c) Salinity of fluids

Resistivity and salinity of pore fluid have an inverse proportionality relationship as described by Keller and Frischknecht (1966) and Didas (2018).

Then, the resistivity is:

$$\rho \approx 10/\text{Concentration} \quad (6)$$

(d) Water rock interaction and alteration

In the presence of water and elevated temperatures, rocks react with water producing alteration minerals characteristic of the formation temperature and rock type. These minerals provide information about the flow paths of the geothermal water as well as the temperatures present (Figure 3). Alteration starts at 50°C and becomes pronounced as temperatures approach 100°C with the formation of low-temperature zeolites and smectite clay minerals making the rocks conductive (Hersir and Árnason, 2013). This is referred to as the smectite zeolite zone.

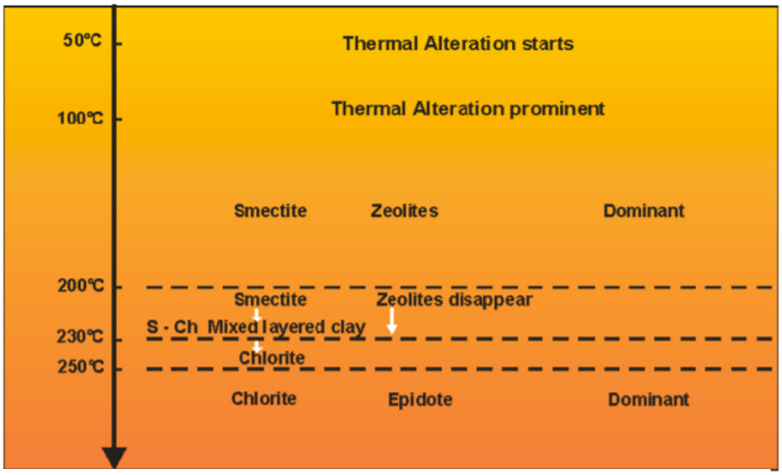

FIGURE 3: Alteration temperatures and mineralogy (Kristmannsdóttir, 1979)

At higher temperatures, in the range of 220-240°C, smectite and zeolites are gradually replaced by chlorite as the dominant alteration mineral in the so-called mixed layered clay zone (Kristmannsdóttir, 1979 in Hersir and Árnason, 2013) and the resistivity increases again. At still higher temperatures (260-270°C) epidote becomes abundant in the so-called chlorite epidote zone. This zoning applies to freshwater basaltic systems. However, in brine systems, the zoning is similar but the mixed-layer clay zone extends over a wider temperature range up to 250-300°C (Árnason et al., 2000 in Kahwa, 2012). In low-temperature geothermal systems (< 180°C) a common alteration mineral is smectite clay which is present in the smectite zeolite zone.

4.2 Resistivity methods

In this section, resistivity methods are discussed by introducing the fundamental principles as well as by describing the field procedures that are involved in acquiring the data, the equipment used and preliminary post field processing of the data. Direct current (DC) methods are not discussed in great detail in this report but the emphasis lies on Magnetotelluric (MT) and Transient electromagnetic (TEM) methods as these are the main methods that were used for acquisition of the data which are discussed here.

4.2.1 DC Methods-Schlumberger soundings

In DC surveys, a direct current is injected into the ground through two electrodes (A and B) and electric field which is dependent on the resistivity of the underlying ground is generated by the current and measured as the voltage between two potential electrodes (M and N) in the middle (Figure 4) (Hersir et al., 2021).

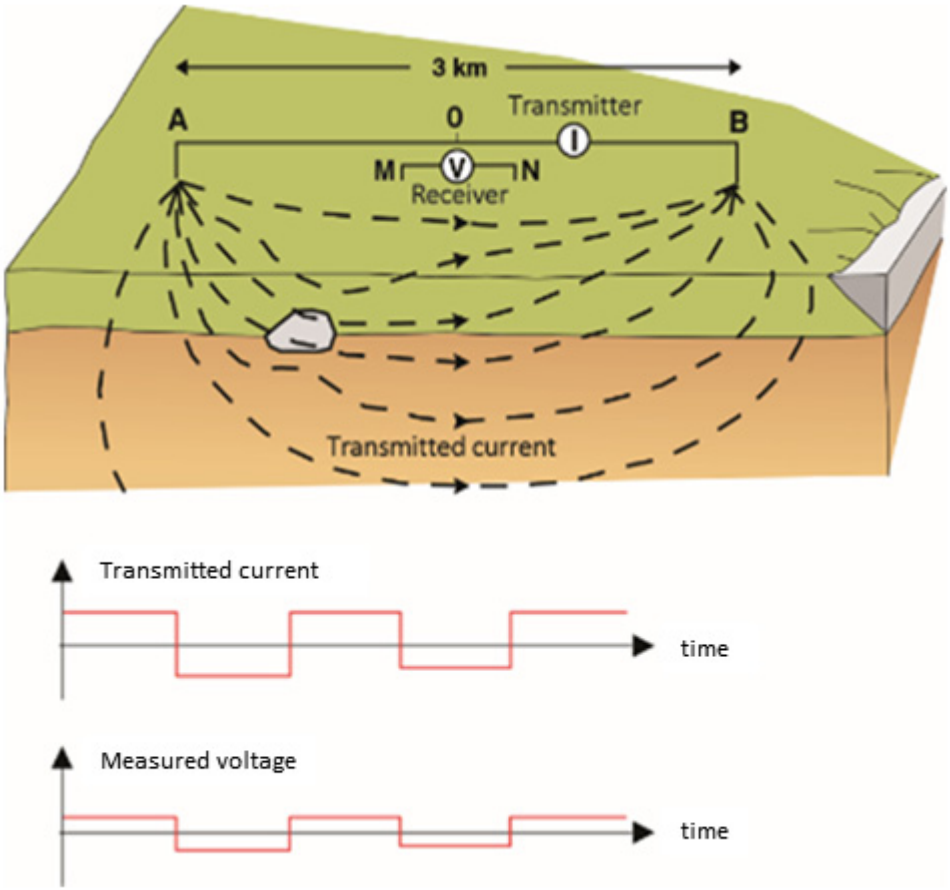

FIGURE 4: Schematic of Schlumberger Array (Hersir et al., 2021)

For a homogeneous Earth and a monopole current source, the electrical potential V_r at a distance r from the current source I is given as follows:

$$V_r = \frac{\rho I}{2\pi r} \quad or \quad \rho = \frac{2\pi r V_r}{I} \tag{7}$$

Where ρ = resistivity (Ωm).

Using equation (7), the apparent resistivity ρ_a can be calculated from the measured potential difference ΔV and the geometrical setup factor K as:

$$\rho_a = \frac{\Delta V}{I}(S^2 - P^2)\frac{\pi}{2P} = K\frac{\Delta V}{I} \quad (8)$$

where S=AB/2, P=MN/2, and K is a geometrical factor. In the case of homogeneous earth equation (8) would give the true resistvity.

As the spacing between the current electrodes A and B is increased, the current penetrates deeper into the subsurface and the measured potential difference at the surface (between M and N) is affected by the resistivity of deeper-lying layers and equation (8) gives an apparent resistivity. In Figure 4, the lower part shows the typical square wave current and the corresponding potential signal. The typical period of the current signal is 1–2 s (Hersir et al., 2021).

4.2.2 Transient electromagnetics (TEM)

The TEM method uses a current transmitted in a source loop to produce a time-varying (controlled source) magnetic field (primary field) to induce currents within the earth (Figure 5). The induced currents produce a secondary magnetic field and the decay rate of the secondary field is measured by induction in a receiver coil. TEM is categorized as an active geophysical method since the primary inducing field is known and can be controlled.

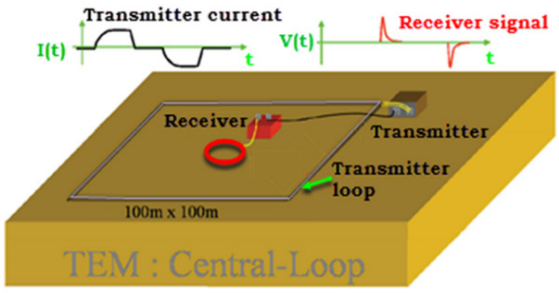

FIGURE 5: Central loop layout (Didas, 2018)

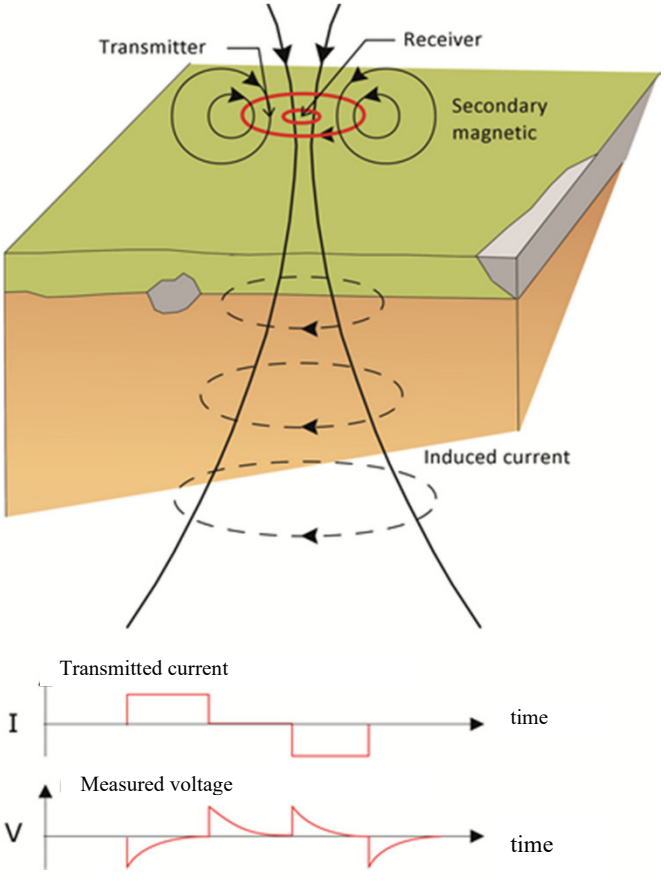

FIGURE 6: TEM setup and propagation of induced currents in the ground

Field Setup

A direct current from a transmitter is fed into a transmitter loop of wire and is abruptly turned off in short time interval. According to Faraday's law, once the current in the loop is turned off, a nearly image of the source current is induced in the subsurface to preserve the magnetic field produced by the original current. Due to ohmic losses, the induced currents decay causing change in the magnetic field which subsequently induces new eddy currents.

The net result is a downward and outward diffusion of currents in the subsurface (Figure 6). The receiver coil measures the induced voltage at different times after the current turn-off. The voltage (decay rate of the secondary magnetic field) depends on the resistivity structure of the earth. TEM surveys allow for probing from near the subsurface to almost one-kilometre depth however this penetration depth depends on the resistivity structure as well as the transmitter loop size and the current.

At "late times" after the current is switched off, an apparent resistivity $\rho_a(r,t)$ (which is the resistivity of homogeneous earth that would give the measured voltage for the specific geometry at time t), can then be calculated using equation (9):

$$\rho_a(r,t) = \frac{\mu_0}{4\pi}\left|\frac{2\mu_0 I A_r n_r A_s n_s}{5t^{5/2}V(r,t)}\right|^{2/3} \quad (9)$$

where μ_0 = Magnetic permeability in a vacuum [H/m];
A_r = Cross-sectional area of the receiver coil [m^2];
A_s = Cross-sectional area of the transmitter loop [m^2];
n_r = Number of windings in the receiver coil;
n_s = Number of windings in the transmitter loop;
V = The voltage response [V], the induced voltage at time t;
I = Current strength [A];
t = Time [s] after current turn-off.; and
r = Radius of the transmitter loop [m].

Contrary to DC methods and MT, TEM suffers minimal distortions due to surface inhomogeneities since the late time signals are little affected by near-surface variations (see discussion of "static shifts" below). Noise sources in TEM soundings are cultural noise such as power lines. The turn-on effect is counteracted in temtd by going backwards in time four cycles of turn on and turn off.

Field setup and data acquisition

The TEM data in this report were obtained using two types of equipment, i.e., the Zonge GDP 32^{24} and the Phoenix, V8 receiver and T4 transmitter (Figure 7).

For Zonge equipment, a source loop of 15625 m^2 and a receiver loop/coil of 10,000 m^2 was used while 10,000 m^2 coincident receiver and source loops were used for the Phoenix setup. The synchronization between the receiver and transmitter was done by radio communication. A square loop of 100 m x 100 m was laid out on the ground. The input current into the source loop was achieved by using a 12 V car battery. The input voltage was amplified by the transmitter to achieve higher voltages.

FIGURE 7: The V8 receiver (a) and T4 phoenix transmitter (b)

Post field processing

Raw data files (*CAC, *TSS) from the receiver are dumped to a field computer and then converted to AVG and USF file formats using the "TEMAVGW" and "WinG link" programme for the Zonge and Phoenix equipment, respectively. *.AVG and *.USF files are further processed by the TemX code that was developed at Iceland Geosurvey, ÍSOR (Árnason, 2006a). This code performs normalization of the voltages with respect to the transmitted current, gain and effective area of the transmitter and receiver loop/coil and then displays all the data graphically, allowing the user to omit outliers. It calculates and averages voltage readings and calculates late time apparent resistivity. The program produces an output file *.inv ready for inversion by the temtd programme. A special script, Zavg2temtd, was also used to convert *AVG files to temtd readable *.inv files in the pre inversion preparation of the Zonge TEM data.

The temtd program also offers the option of performing a minimum structure (Occam) inversion where the thickness of the resistivity layers is fixed and increases exponentially with depth. Typical inversion results/models from Occam 1D inversion of TEM data are shown in Figure 8.

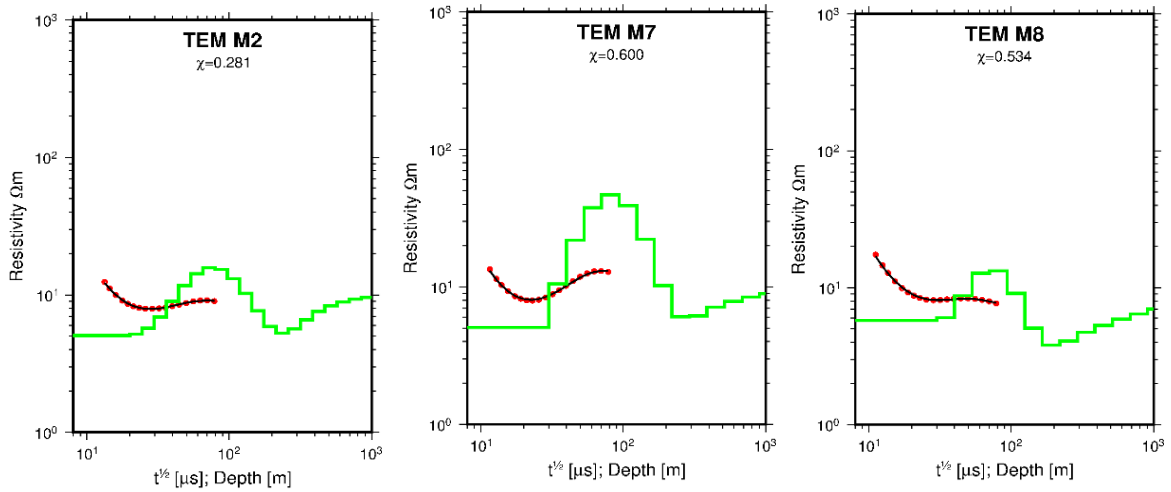

FIGURE 8: 1D inversion of three TEM soundings, M2, M7 and M8, from the Buranga prospect. Red dots are the measured apparent resistivity values, the black line shows the calculated apparent resistivity from the 1D model in green, and χ is the RMS misfit between the measured and calculated data from the model.

4.2.3 Magnetotellurics (MT)

During the last half-century, a rapid development of MT, one of the strongest techniques for resistivity surveying has taken place. It is a passive method where the natural time variations in the Earth's magnetic field, the so-called micro pulsations (Hersir et al., 2021), are the signal source that is used to infer subsurface resistivity structures down to several kilometres depth, depending on the period. Time series/variations of the electric field E due to telluric currents induced in the ground at the surface and the magnetic field H are measured at the surface. The time series are, by Fourier transformation, turned int frequency (ω) domain and the relation between E(ω) and H(ω) expressed in terms a frequency dependent tensor Z(ω) which is dependent on the sub-surface resistivity and can be used to calculate apparent resistivity as a function of the frequency.

In processing of MT data, the recorded time series data are Fourier transformed from the time domain into the frequency domain and the cross and auto powers of the fields are calculated to give the impedance tensor as a function of the period of the electromagnetic fields. A solution that describes the relationship between the electric and magnetic fields can be expressed through equation (10):

$$\begin{bmatrix} E_x \\ E_y \end{bmatrix} = \begin{bmatrix} Z_{xx} & Z_{xy} \\ Z_{yx} & Z_{yy} \end{bmatrix} \begin{bmatrix} H_x \\ H_y \end{bmatrix} \tag{10}$$

Or in matrix notation as

$$\vec{E} = Z\vec{H} \tag{11}$$

Where, $\vec{E}$ = Electric field vector;
$\vec{H}$ = Magnetic field vector; and
Z = Complex impedance tensor related to the subsurface resistivity structure.

We also measure the vertical component of the magnetic field H_z which is sensitive to currents in the ground and their directionality.

For a homogeneous and 1D (layered) Earth, $Z_{xy}=-Z_{yx}$ and $Z_{xx}=Z_{yy}=0$. For a 2D Earth, that is, resistivity varies with depth and in one horizontal direction, it is possible to mathematically rotate the coordinate system such that $Z_{xx}=Z_{yy}=0$, but $Z_{xy}\neq-Z_{yx}$. For a 3D Earth (resistivity varies in all three directions), all the impedance tensor elements are different.

From the impedances, the apparent resistivity ρ and phases θ for each period T (inverse frequency) are calculated according to the following equations:

$$\rho_{xy}(T) = 0.2T\left|Z_{xy}\right|^2 = 0.2T\left|\frac{E_x}{H_y}\right|^2 ; \theta_{xy} = \arg\left(Z_{xy}\right) \quad (12)$$

$$\rho_{yx}(T) = 0.2T\left|Z_{yx}\right|^2 = 0.2T\left|\frac{E_y}{H_x}\right|^2 ; \theta_{yx} = \arg\left(Z_{yx}\right) \quad (13)$$

In a homogeneous earth, all currents, electric fields, and magnetic fields are horizontal regardless of the direction from which these fields enter the earth. This is because of the high conductivity of the earth relative to the air (Vozoff, 1972; Kahwa, 2012).

A measure of the depth of penetration in MT surveys is given by what is referred to as skin depth. The penetration depth δ is the depth where the EM fields have attenuated by a factor of e^{-1} (about 0.37) of their surface amplitude. The skin depth δ depends on the period **T** of the wave and the resistivity ρ of the subsurface through which the wave is propagating. For a homogeneous earth with resistivity ρ is given as:

$$\delta(T) \approx 500\sqrt{T\rho} \quad \text{(m)} \quad (14)$$

The longer the period T, the greater the depth of penetration and vice versa. Therefore, deep mantle studies are conducted by recording data for several weeks to achieve the desired long periods and penetration depth. However, for geothermal exploration purposes, recording is usually done for about 20 hrs per station.

MT data in geothermal exploration are generally in the frequency ranges from 400 Hz (0.0025s) to about 0.001 Hz (1000s). The short-period MT data (high frequency) mainly reflects the shallow structures due to their short depth of penetration while the long-period data reflect the deeper structures.

MT field setup and data acquisition

The Buranga MT data was collected in three different campaigns in 2016, 2017 and 2019 by staff from GRD. Magneto-telluric data acquisition in the Buranga prospect was done using the five-component data acquisition (MTU-5A) instrumentation from Phoenix geophysics, a Canadian based geophysical company (Figure 9). It is relatively light equipment weighing about 4 kg and consisting of three magnetic field channels/sensors, Hx, Hy, and Hz, and two (2) electric field channels, Ex and Ey (Figure 10a). The recorder has a 130 dB dynamic range with a gain that can be varied by a factor of 4 and also has an inbuilt power line notch filter of >40dB. Each MTU box comes with two MTC-50H and one AMT-30 induction coils and five non-polarising porous pot electrodes.

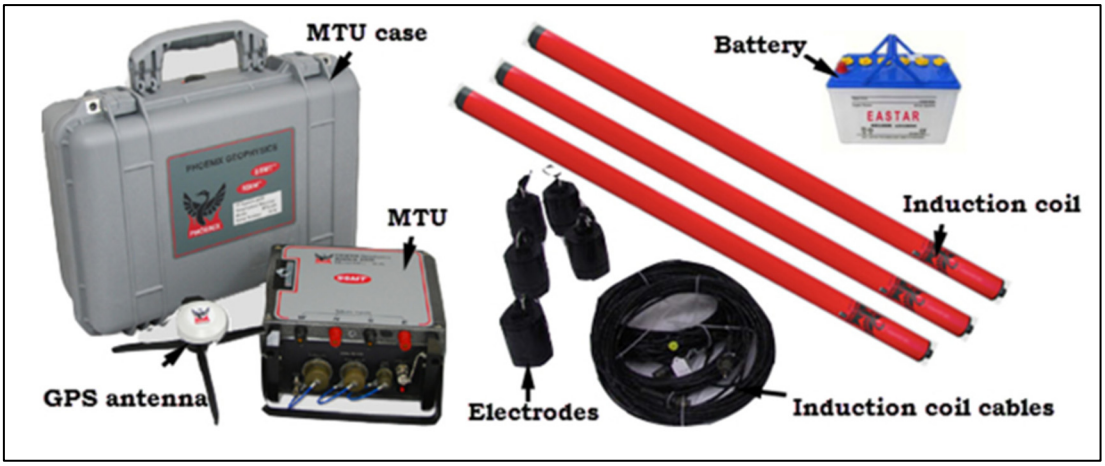

FIGURE 9: Instrumentation for a typical MTU-5A Station (modified from Phoenix, 2018)

Before the equipment is deployed for data acquisition, the MTU boxes as well as the induction coils are calibrated (Figure 10b) near or within the survey area to create start-up table files that contain equipment and site-specific parameters as well as looking at the amplitude response curves of the coils and boxes to ensure that they are in good conditions. The porous pot electrodes are usually checked using a multi-meter and paired according to the static voltage that they generate between themselves.

In the field setup, the MTU data datalogger is placed at the centre of the sounding and grounded with a porous pot. The electric field components Ex and Ey are measured using an electric dipole of two porous pot electrodes while the magnetic components are measured using three induction coils, Hx and Hy for the horizontal field and Hz for the vertical field. Hx and Hy are both horizontal but perpendicular to each other, normally magnetic N-S (x) and E-W (y), respectively. The porous pot electrodes are buried into the ground and contact resistance is improved by pouring water or adding some bentonite clay solution in case the ground is very resistive.

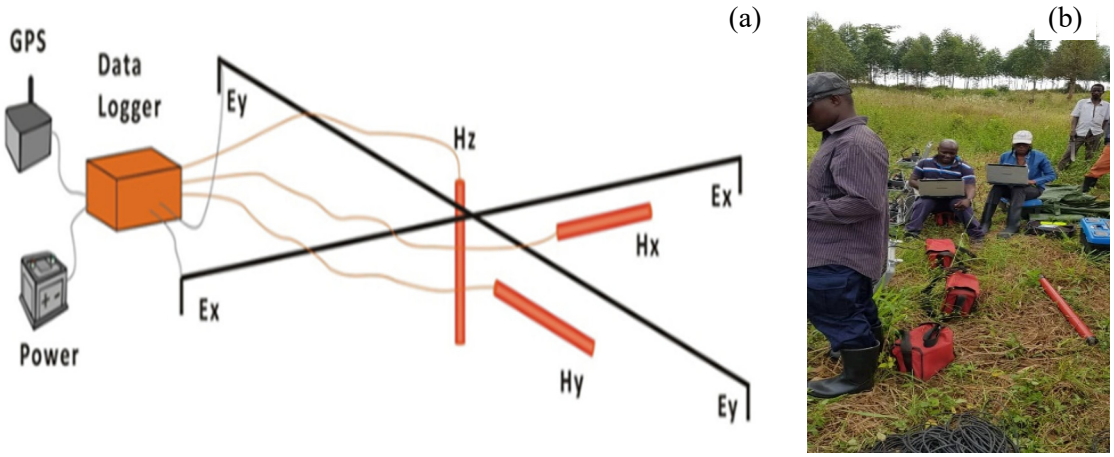

FIGURE 10: (a) Layout of an MT sounding (Flóvenz et al., 2012 in Kahwa, 2012); (b): Field crew preparing for sensor and box calibration

The induction coils are oriented with the head (end of coil) facing north for Hx, facing east for Hy and facing down for Hz. They are buried and levelled to minimise noise caused by shaking of the trees or vegetation. Vibration of the coils causes unwanted noise in the data.

CF (storage data) cards containing the start-up table are inserted into the MTU box and acquisition is started. When the acquisition is done, the CF cards are removed from the box and recorded time series data are damped onto a field computer for storing and processing.

Post-field processing and inversion

Time series (TSER) data (raw MT data) were available for data collected in 2016 and 2019 whereas processed *.edi (electrical data interchange standard) files were available for data collected in 2017. The processing software used here is from Phoenix Geosystems. Using the Synchro time-series view program (Figure 11), time series are graphically viewed as a preliminary quality check of the data. This helps identify bad channels or channels that were completely off during acquisition.

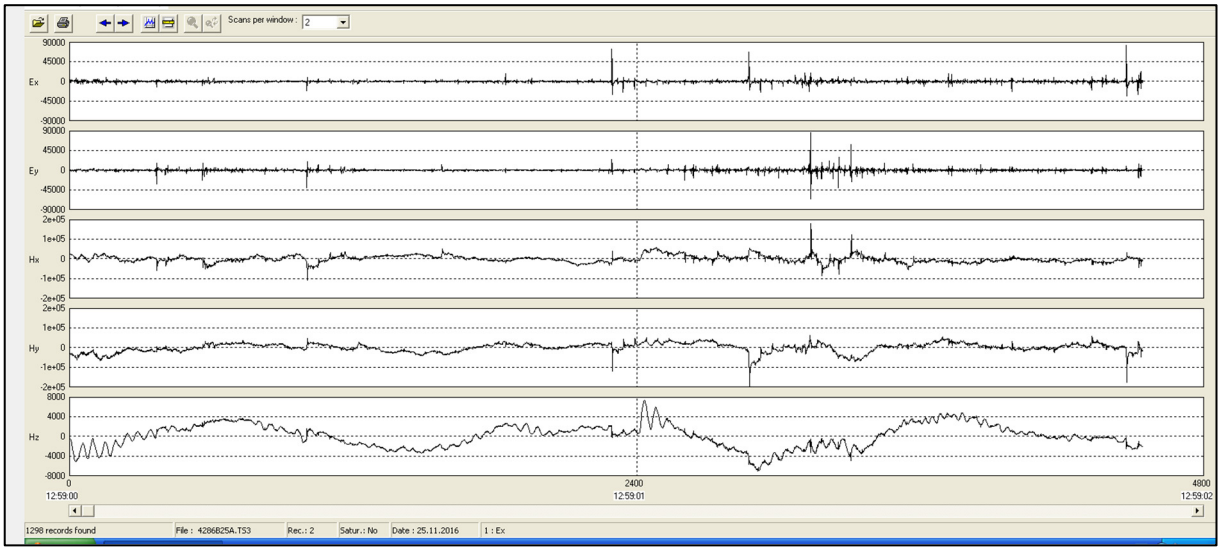

FIGURE 11: Synchro time series view of data collected on 25-11-2016 displaying the first two electric components Ex and Ey and the three magnetic channels Hx, Hy, and Hz

The time-series data were processed using the Windows XP based SSMT 2000 software that is provided with the MT equipment. For every station, *.TBL files are reviewed or edited to help input or correct parameters such as site name, electric dipole lengths, coil orientations, serial numbers, and site layout crew.

Fast Fourier Transformation of the TSER data converts time series to frequency domain. Then auto and cross spectra segments, which are products of the field components, and their complex conjugates are calculated for both high (MTH) and low (MTL) frequencies.

Using the MT-Editor software, the MTH and MTL files are edited (discarding outliers) to evaluating apparent resistivity and phase until satisfactory smooth data curves are obtained. The editing was done by eliminating noisy sections of the curves and outlying data points and finally exported as *.edi files ready for the next step, that is 1D inversion using the temtd software.

When the *.edi files are prepared they are further handled in the Linux environment. Using special Linux based commands such as spect2edi, edi2edi, the original *.edi are transformed into *.EDI. These commands calculate other MT parameters from the spectral matrix such as impedance rotation angles, tipper, phase, apparent resistivity, Zstrike, ellipticity, Tstrike, skew and errors (Figure 12) which might be absent in the original *.edi file from SSMT2000.

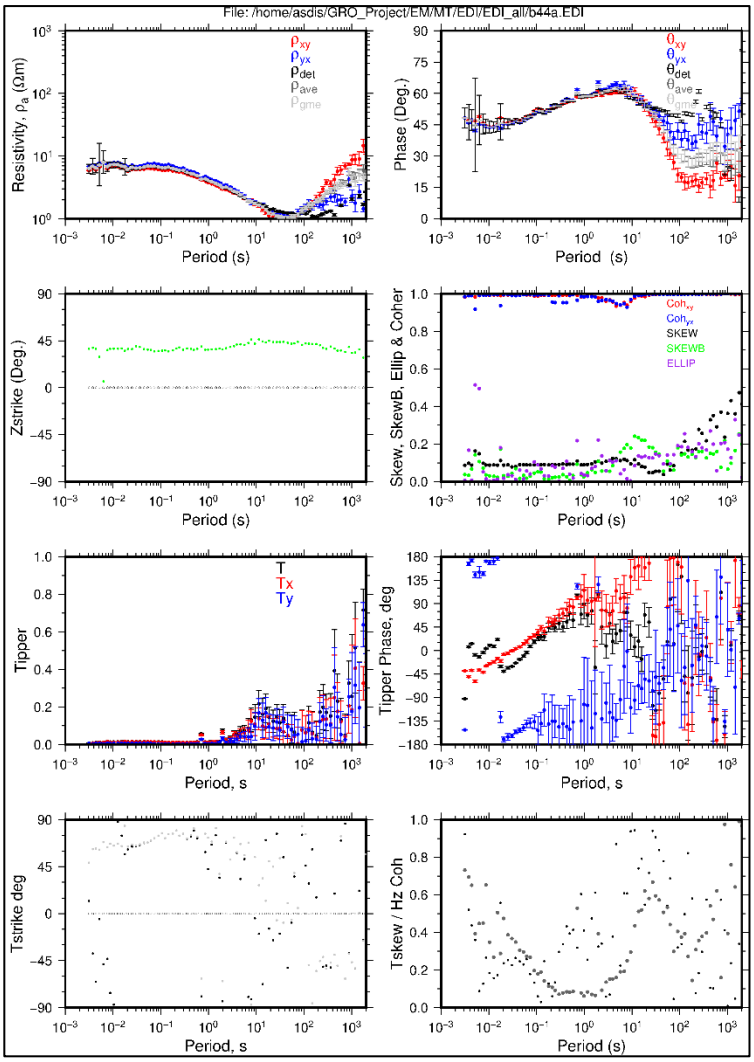

FIGURE 12: Output from the MT processing showing parameters calculated from the spectral matrix of the *.edi

Figure 12 shows graphical display of the main parameters derived by processing from the raw data. Different apparent resistivity curves are plotted in the apparent resistivity panel on the top left in Figure 12. This helps to get a first impression of the subsurface resistivity. The dimensionality of the resistivity structure and strike is indicated by Zstrike and Skew. For a purely 1D response (layered earth), all the apparent resistivities and phases would have a similar Zstrike value and all the invariants would have a similar value (Park and Livelybrooks, 1989 in Didas, 2018).

For the Buranga area, the rotationally invariant determinant was inverted for most of the soundings except those where the determinant could not be calculated, i.e., stations like B54, b75a, and BUR005.

Although MT is considered the most powerful resistivity technique, it is however not free of problems which the geophysicist should bear in mind. Three major problems affect MT data measurements:

(a) The Dead bands

These are the frequency bands between 0.5 and 5 Hz (for MT) and between 1 and 5 kHz (for AMT) on the electromagnetic spectrum. Of these, 1 to 5 kHz is the most serious. It is caused by low amplitude of ionospheric currents in this frequency range. Noise due to wind is often high in these bands causing a low signal to noise ratio.

(b) Cultural noise

Electromagnetic signals at the surface of the earth are of various origins. The sources for MT are the natural variations in the earth electromagnetic field. “Man-made” signals from local activities like power lines, communication masts and moving vehicles, etc. are noise to the MT.

To minimise this problem, many authors (e.g., Gamble et al., 1979; Clarke et al., 1983) have proposed a method of processing MT data using a remote reference site together with the MT data from the survey area assuming that the cultural noise is not correlated between the two sites. The remote reference is usually some tens of kilometres away at a quiet location. This technique has proven to be quite useful and is recommended for all MT surveys since it helps reducing the influence of local noise in the data considerably.

(c) The Static shift

Static shift is an integral uncertainty in the MT data that is mainly due to local near-surface resistivity inhomogeneities and topography. MT and DC methods generally suffer from this problem because they rely on measuring electric field or voltages over short distances at the surface (Árnason, 2015).

Static shift manifests itself in the parallel shift of the apparent resistivity curves when plotted on a log scale, i.e. a constant multiplicative factor S of the apparent resistivity values independent of frequency. Thus, the correct level can be located somewhere above, below or in between the measured responses if the two polarizations are shifted differently. If uncorrected for, this shift will introduce unrealistic structures in the final inversion models. However, it is important to note that the shift only affects the apparent resistivity and not the phase curve (Jones and Groom, 1993), but the phase lacks information on absolute resistivity values. Apart from topographic distortions, there are two main reasons for MT static shift:

(i) Current distortion (Current channelling)

This is mainly due to superficial bodies that distort the current distribution hence distorting the electric field, causing the impedance magnitude to increase or decrease by a scaling factor. This factor shifts the apparent resistivity curve on logscale as mentioned earlier.

Consider a superficial body of resistivity ρ_2 which is lower than the resistivity of the surrounding ground ρ_1. Considerable amounts of the current will be channelled through the body due to its low resistivity reducing the current density (and voltage difference) at the surface. However, if $\rho_2 > \rho_1$, then all the current will be repelled away from the body leading to increased current density at the surface. This is referred to as current distortion (Figure 13).

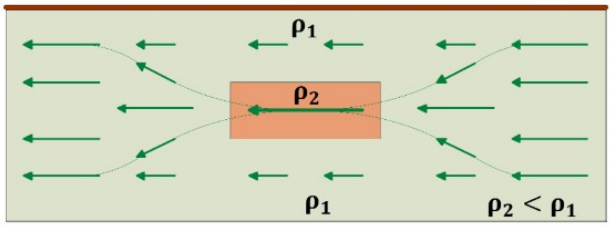

FIGURE 13: Current distortion (Árnason, 2008)

(ii) Electric field Distortion

In this case, due to the vertical resistivity discontinuity at the surface, the electric field (voltage difference over a given length) is lower in the low resistivity domain. Resistivity discontinuities like the ones shown in Figure 14 cause local distortion of the amplitudes of electric fields as a result of conservation of electric current, hence causing impedance magnitudes to be enhanced or diminished by real scaling factors.

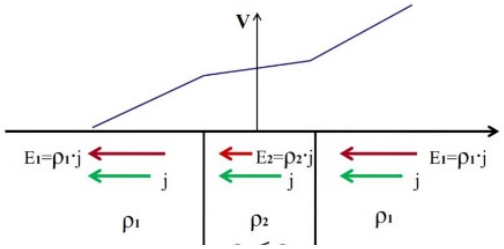

FIGURE 14: Electric field distortion (Árnason, 2008)

At late times, the apparent resistivity from TEM is independent of near-surface structures. The most common and reliable method to correct for MT static shift is the one that uses a co-located central loop TEM sounding and jointly inverting it with the MT data and adjusting the shift multiplier S as well as the resistivity model.

4.3 Joint inversion and static shift correction

The program temtd can be used to invert TEM and MT data separately or do joint inversion of both MT and TEM. For this report, only twelve TEM stations were inverted separately using the UNIX/LINUX based temtd program which is capable of performing both Occam and layered inversions. According to Árnason (1989), the inversion is based on the Levenberg-Marquedt nonlinear least square inversion.

The misfit measure is the root mean square difference, χ, between the measured and calculated values, weighted by the standard deviation of the measured value. Resistivities and thicknesses of discrete layers are calculated using both amplitude and phase as input. Smooth models with respect to resistivity variations between layers and layer thicknesses can be achieved by using the damping factors which counteract sharp steps and oscillations in the model values.

Static shift multiplier

Static shift multipliers for 63 MT stations were determined by joint inversion with co-located TEM soundings. As shown in the histogram in Figure 15, 37 stations had a multiplier in the range of 0.5-1.0, meaning that apparent resistivity curves for these stations were shifted down (shift multiplier <1). The shift could be attributed to topographic effects of the Rwenzori ranges that can cause telluric distortions (Didas, 2008). Soundings on the relatively homogeneous sedimentary plain were assumed not to have much static shifts and hence they were inverted separately without the TEM. It is, however, recommended by the author to carry out infill TEM surveys at locations with only MT stations to fully constrain the inversion and eliminate any possibility for static shift.

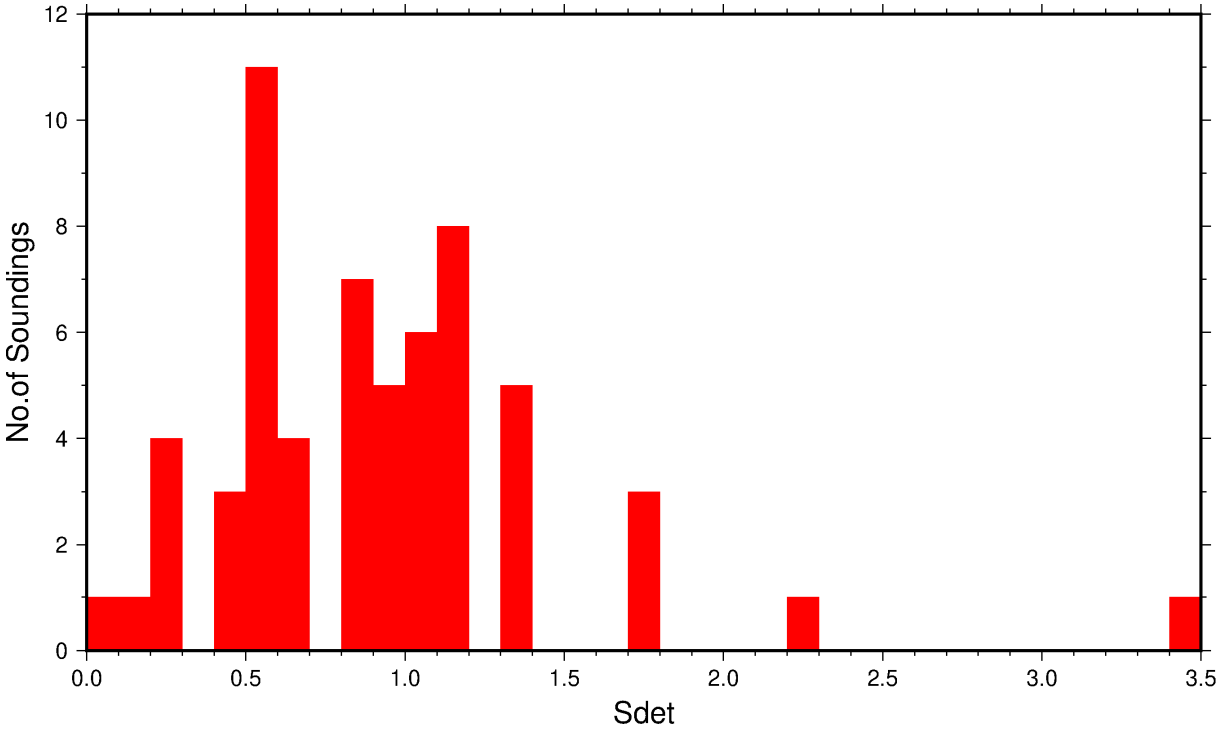

FIGURE 15: Static shift multiplier Histogram for Buranga

Based on the static shift multiplier results, another 54 MT sounding were inverted alone and also twelve TEM soundings were inverted as stand alone. 1D inversion of MT and TEM data was carried out using the temtd inversion program which has the capability to graphically display the data during the inversion process. The rotationally invariant determinant MT apparent resistivity was inverted by (smooth) Occam inversion with the most appropriate model parameters until a good fit between measured and calculated the TEM and the MT data was obtained. Examples of the joint inversion are shown in Figure 16 and 17.

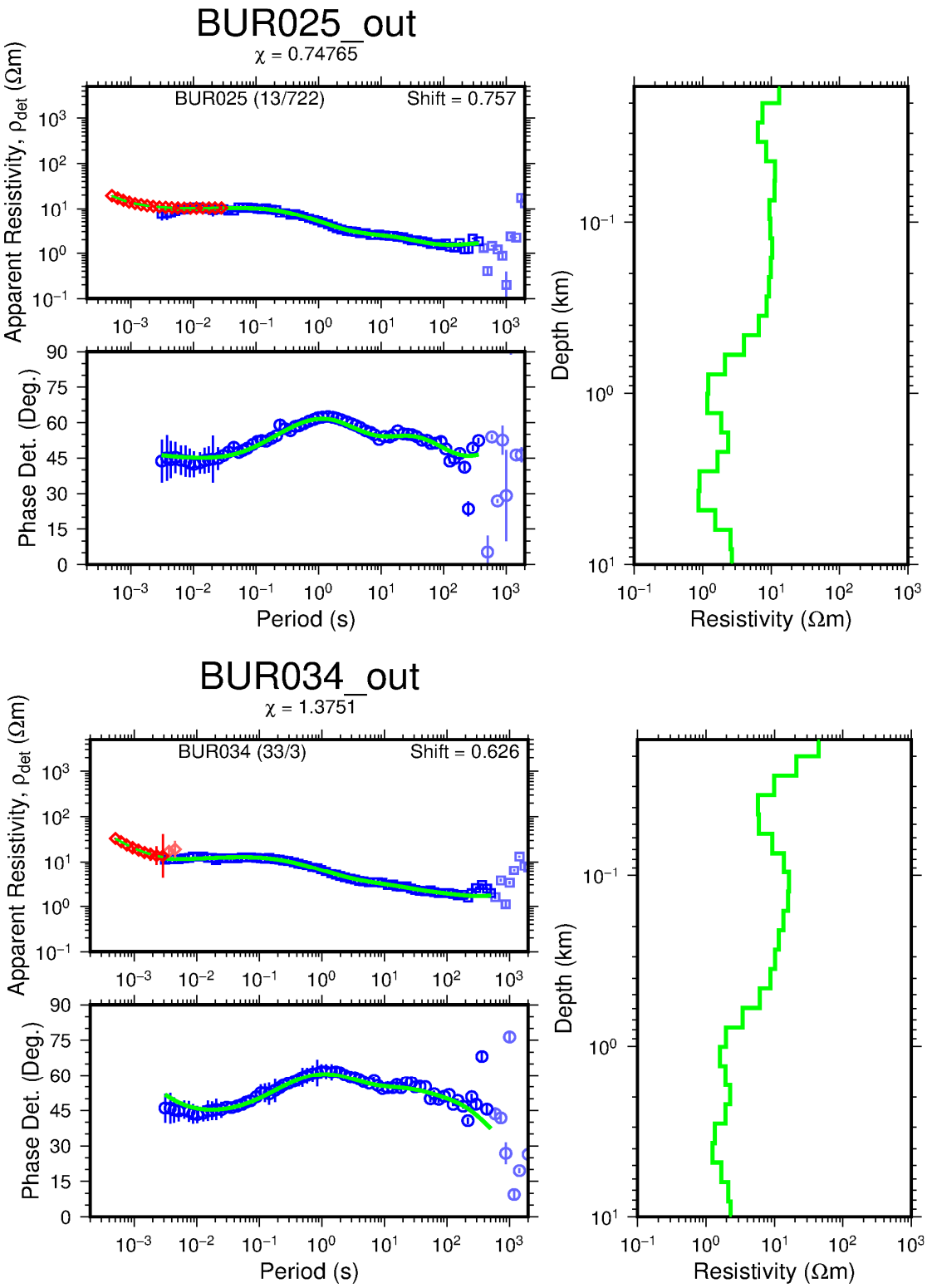

FIGURE 16: Results of Joint inversion from two MT stations with two co-located central loop TEM soundings. The plot shows the measured MT data (blue squares) phase (blue circles) together with the resultant inverted phase and apparent resistivity curves (solid green), a 1D Occam inversion model (right) and the co-located TEM curve (red diamonds)

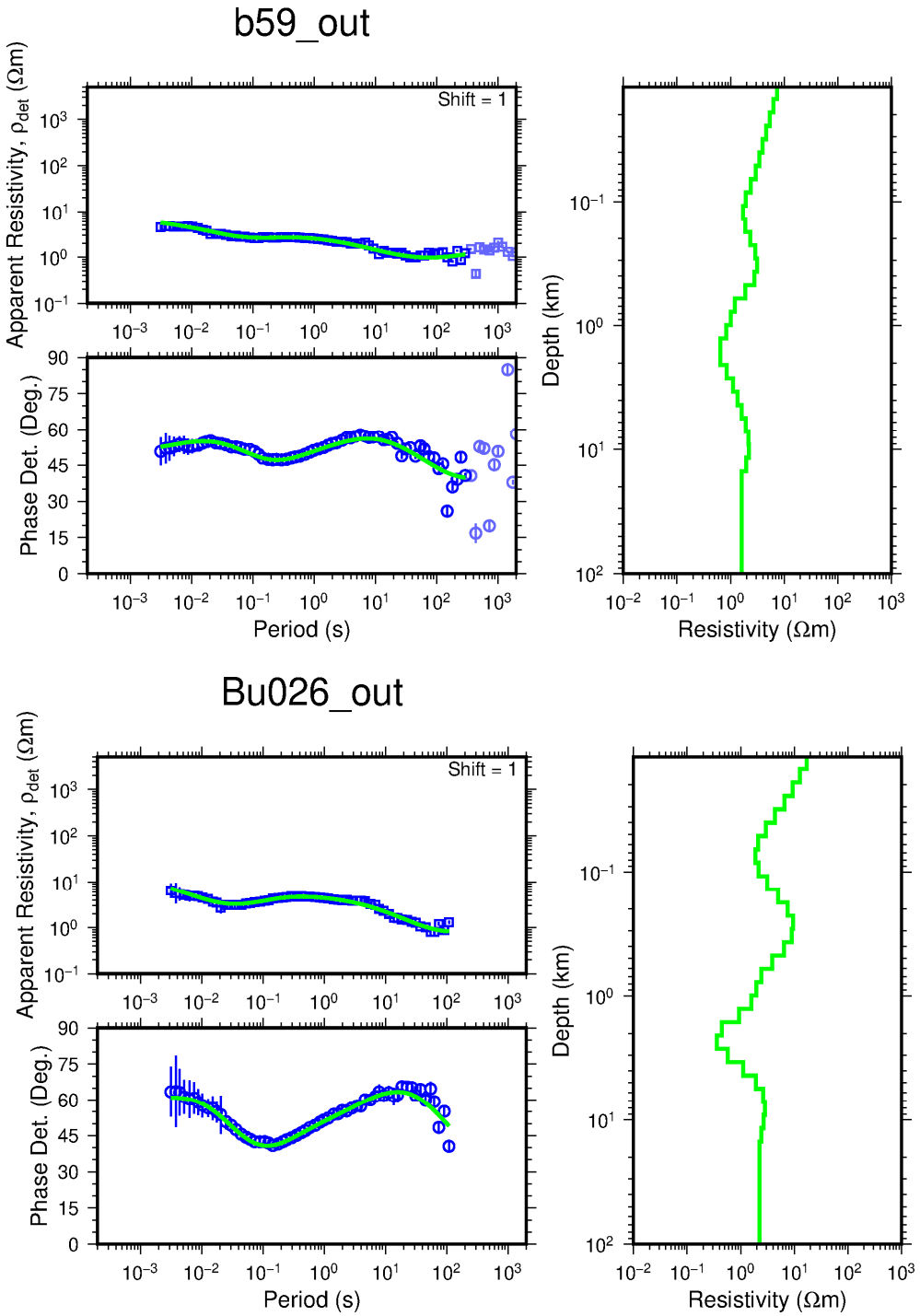

FIGURE 17: Example of the results from MT inversion alone. Inversion outputs of apparent resistivity and phase curves are shown in green solid lines on the left while 1D resistivity depth models are shown in light green curves on the right. Original resistivity and phase data are shown on the left by blue squares and circles, respectively.

5. RESULTS AND INTERPRETATION

5.1 Strike analysis

In electrical strike analyses, the MT data are mathematically rotated from the measurement layout coordinate system to minimise the diagonal elements of the impedance tensor. In the rotated coordinated system the x-axis (Z-strike) is parallel or perpendicular to main resistivity boundaries (main geological features). Weather it is parallel or perpendicular, can be resolved by analysing the relation between measured vertical (Hz) and the horizontal (Hx and Hy) magnetic fields and expressed as induction arrows or T-strike. In a 2D earth model, the resistivity varies with depth and in one of the two principal horizontal directions. The strike direction is represented by the induction arrows (perpendicular to strike), strike rose diagrams (Tstrike and Zstrike) and phase tensor diagrams generated from the vertical magnetic field Hz and the phase tensor for each MT station.

5.1.1 Phase tensors

The phase tensor in MT expresses the relationships between the phases of the magnetic and electric fields with period (depth). The advantage of the phase tensor is that it is independent of the galvanic distortion of the electric field and preserves the regional information (Caldwell et al., 2004).

For 1-D regional conductivity structures (resistivity varies only with depth), the phase tensor is characterized by a single invariant phase equal to the 1-D impedance tensor phase (phase ellipse is almost a perfect circle) (Figure 18). If the regional conductivity structure is 2-D, the phase tensor is symmetric with one of its principal (long) axes aligned parallel to the strike axis of the regional structure. Therefore, the skewness or asymmetry of the phase tensor can be used to determine the dimensionality of the subsurface structure.

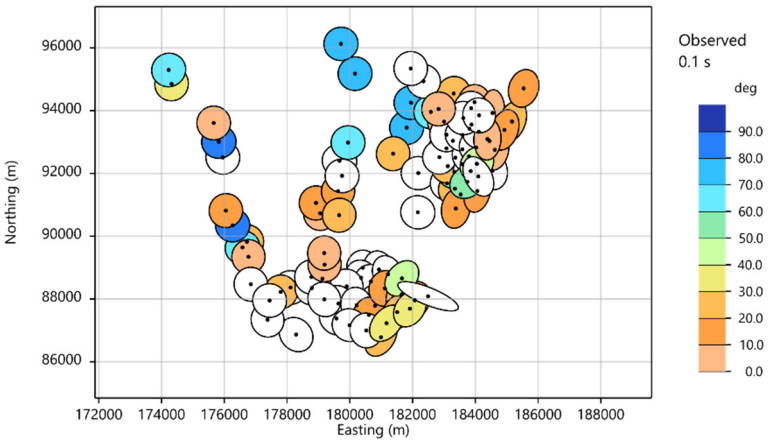

FIGURE 18: Phase tensor ellipses at 0.1 s plotted based on angle α

The ellipses are plotted with the principal phases (PhiMin and PhiMax) as the semi axis and with the orientation Alpha-Beta expected to reflect the regional strike direction. The colour fill, Phi2 is set such that it's the geometric average of the principal phases, and is thus a representative phase for the impedance tensor (Geotools, 2019).

MT Phase tensor analysis for periods of 0.1 s, 1 s, 10 s and 100 s was done using an interpretation / visualization software called **Geotools**.

In the phase tensor analysis shown in Figures 18 and 19, the data show 1D characteristics near the surface whereas at 100 s, the dimensionality changes to 2D or 3D. This indicates that at depth, there is a controlling strike in the area that is trending in NE-SW direction. More tensor diagrams for other periods are shown in the appendix.

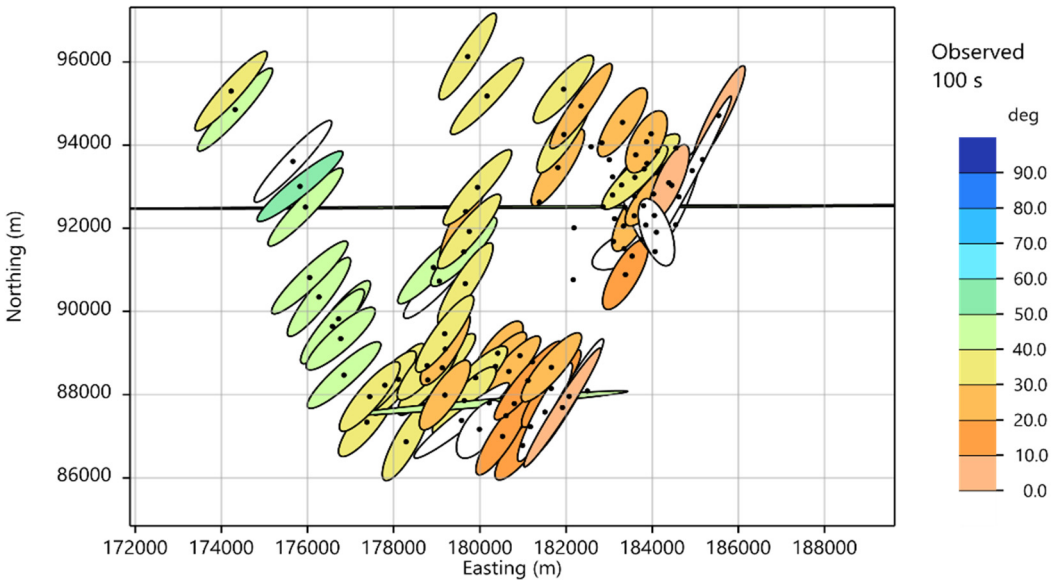

FIGURE 19: Phase tensor ellipses at 100 s, plotted by angle α, the ellipses are aligned in NE-SW direction. The black dots are the MT soundings (coordinates are in UTM zone 36N)

5.1.2 Tstrike and Zstrike

The description of the Tstrike and Zstrike presented here is based on the publication by Hersir et al. (2021). Electrical strike analysis of MT data indicates the directions of resistivity contrasts which are often due to geological structures but are not necessarily seen on the surface. In addition to the resistivity structures below and around the site, the elements of the MT impedance tensor depend on the orientation of the x and y directions of the field layout.

For a 2D Earth, the resistivity varies with depth and in one principal horizontal direction. The horizontal angle perpendicular to that direction is called the electrical strike. The angle it makes with geographical north is called Swift angle or Z-strike Φ (Hersir et al., 2021). It is possible to rotate the coordinate system by mathematical means and recalculate the elements of the impedance tensor for any desired direction. This makes it appear as though the fields (E and H) had been measured in these rotated directions. If the Earth is 2D and the coordinate system of the field layout has an axis parallel to the electrical strike direction, we have **Zxx = Zyy = 0, but Zxy ≠ Zyx.**

From the rotated tensor we get two sets of apparent resistivity (ρ_{xy} and ρ_{yx}) and two sets of apparent phases (θ_{xy} and θ_{xy}). For a 1D Earth, they are equal. The electrical strike or Z-strike can be determined by minimizing ($|\mathbf{Zxx}|^2 + |\mathbf{Zyy}|^2$) with respect to Φ, the rotation of the coordinate system. There is, however, a 90° ambiguity in the strike angle determined in this way because the diagonal elements of the tensor are minimized if either the x- or y-axis is along the electrical strike. There is, therefore, no way of distinguishing between Φ and Φ+90° from the impedance tensor alone. The depth of investigation increases with period and Z-strike commonly depends on the period.

Consequently, the dominant electrical strike can be different at different depths, reflecting different structures at different depths. A Z-strike map at 1 – 10 s is shown in Figure 20.

Another parameter that is used to analyse directionality is the so-called tipper T, which relates the vertical component of the magnetic field to the two horizontal components:

$$Hz = TxHx + TyHy \tag{16}$$

Where Tx and Ty are the x and y components of the tipper, respectively.

For a 1D earth, the tipper value is zero, i.e Tx = Ty = 0. For a 2D Earth, the coordinate system can be rotated so that the x-axis is in the strike direction so that Tx=0 but Ty≠0. This is done by minimizing |*T*x|. Unlike Zstrike, Tstrike does not suffer the 90° ambiguity.

The tipper can be represented by two real vectors, the real and imaginary part. The real arrows point away from a zone of low resistivity at sufficiently low frequencies and towards a zone of higher resistivity. The length of the arrows indicates the size of the resistivity contrast. For a 2D Earth, the real and imaginary arrows are collinear and point perpendicular to the geo-electrical strike (Berdichevsky and Dmitriev, 2008; Hersir et al., 2021). A Zstrike and Tstrike map at periods of 1-10 s is shown below (Figure 20 and 21). More maps at different periods are shown in the appendix of this report.

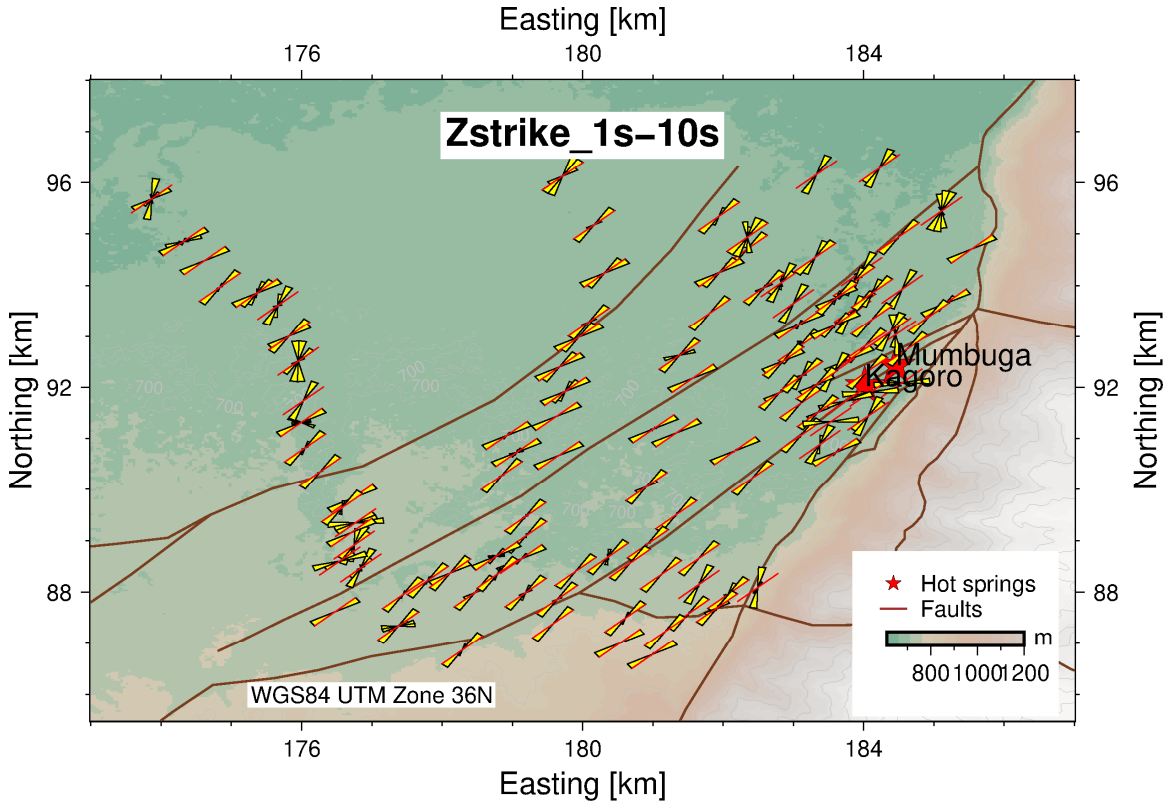

FIGURE 20: Zstrike map for Buranga prospect for the period 1-10 s

Strike analysis (Figures 20 and 21) maps at periods of 1-10 s show an alignment of a deep NE-SW controlling structure in the Buranga area where we have the major controlling faults. This alignment agrees with the location of the surface manifestations which are found approximately along a line striking about N20°E, sub-parallel to the local (Bwamba) fault. This indicates that the resistivity changes the least in NE-SW direction but changes considerably perpendicular to the faults.

5.1.3 Induction arrows

Another way of displaying the tipper is to plot "induction arrows" (Figure 22). The induction arrows are drawn from the real and imaginary parts of the tipper components. The induction arrows are small on the sedimentary plain, real and imaginary arrows are collinear, being perpendicular to the strike of the two-dimensional structure. Where not small, the real arrows point towards a zone of lower conductivity (by the convention of Berdichevsky and Dmitriev, 2008) allowing the identification of a conductivity structure.

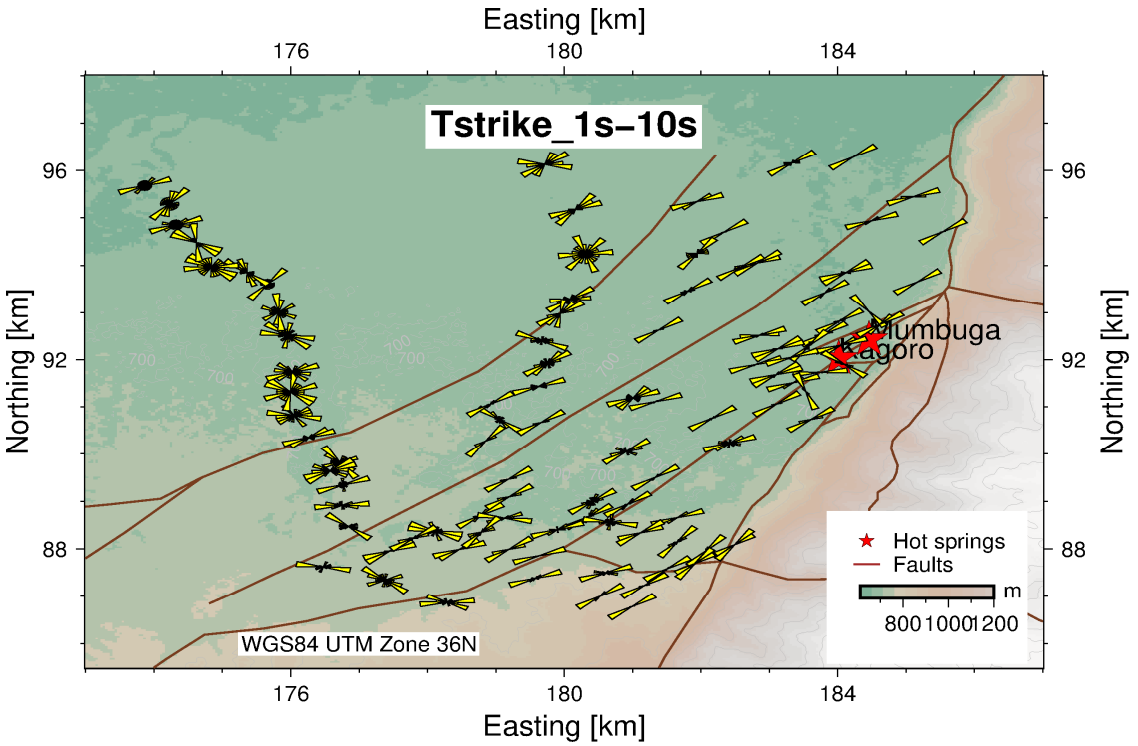

FIGURE 21: Tstrike map for Buranga prospect for the period 1-10 s

According to Berdichevsky and Dmitriev (2008), the imaginary part of the induction arrows is sensitive to resistivity contrasts close to the measurement site while the real part is more sensitive to regional resistivity contrasts.

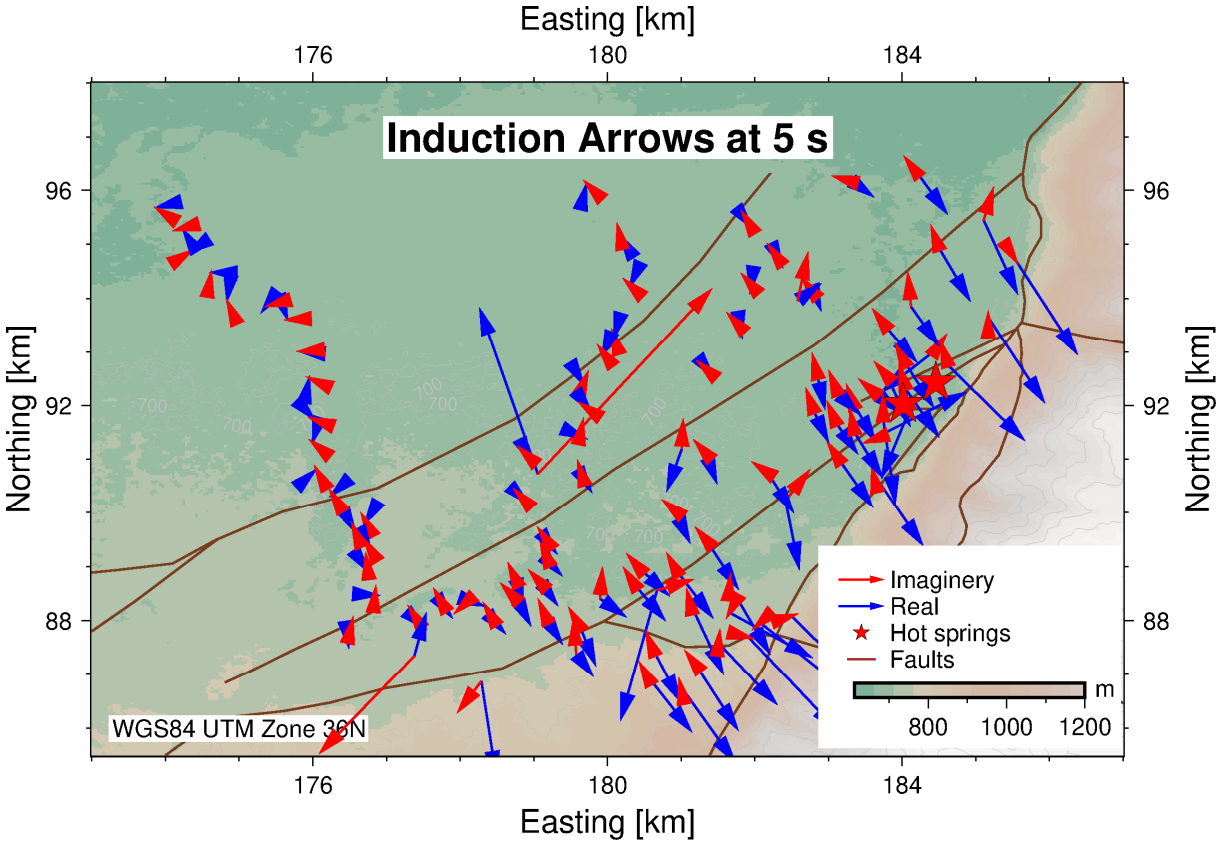

FIGURE 22: Induction arrows for the period of 5 s (Berdichevsky convention)

5.2 Resistivity depth slices

Figure 23 shows the location of MT and TEM soundings in Buranga. Resistivity slices at different depths were generated using the Temresd program developed at ISOR. Such slices help to understand the general lateral trend of the resistivity at different depths below the surface. Figure 24 and Figure 25 show four out of the many depth slices that were produced (for more depth slices see the appendix).

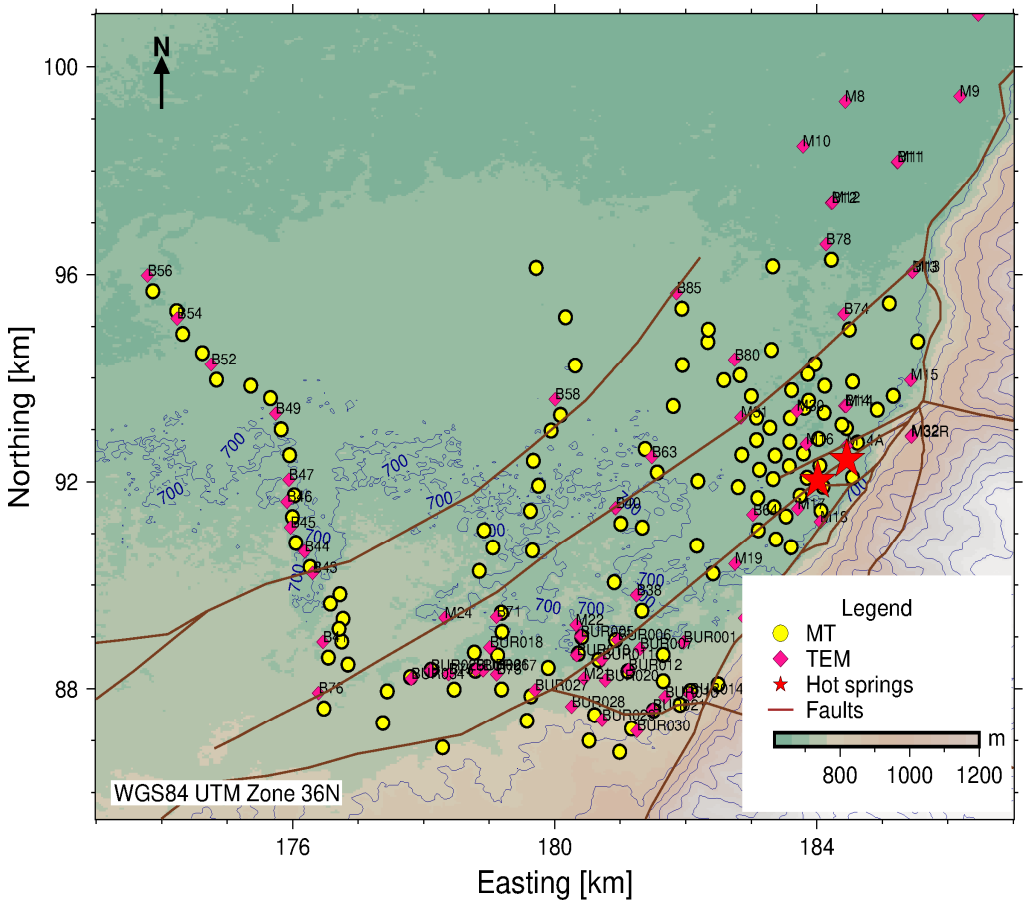

FIGURE 23: Locations of TEM (pink) and MT (yellow) soundings at Buranga prospect

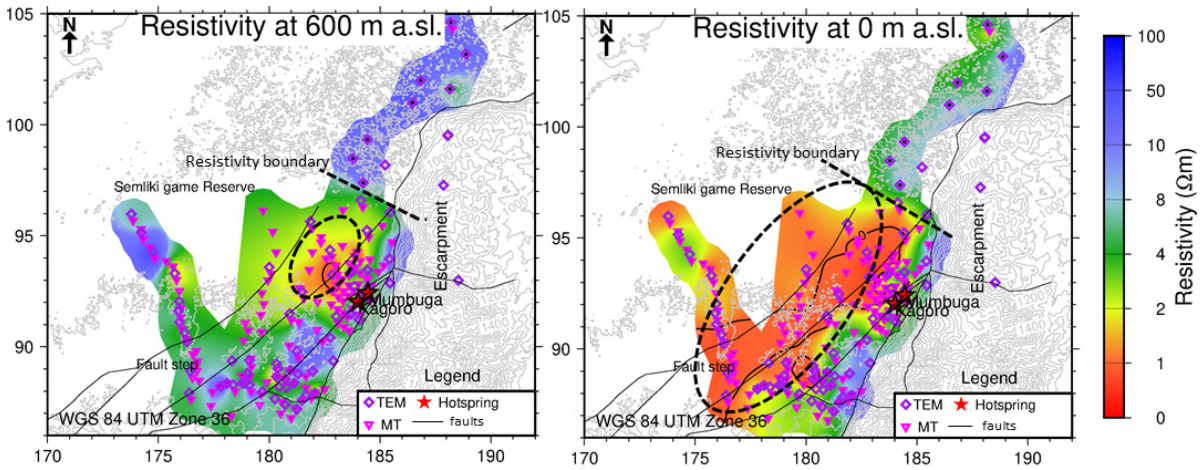

FIGURE 24: Resistivity depth slices at 600 m a.sl. (left) and at sl. (right). Coordinates are UTM (zone 36) in km. Black dotted line represents a probable fault and oval dotted conductive zones a resistivity boundary

The resistivity depth map (Figure 24) at 600 m.a.s.l (about 50-100 m below surface) shows a conductive zone of about 2-4 Ωm (marked in black stippled oval) around the hot springs and resistivity of >10 Ωm towards the NE with a clearly defined and sharp boundary north of the surface manifestations which might be an indication of a contact zone probably due to a cross cutting fault (straight stippled line) trending almost E-W. There is also a high resistivity structure with 8-10 Ωm in the far east, towards the Rwenzori massif.

On the right in Figure 24, resistivity at sea level, the conductive zone increases in size, now covering most of the centre of the prospect area, starting at the border between the massif and the sedimentary plain in the west. This could indicate conductive geothermal fluids within the sediments flowing west ward.

Resistivity depth slices at 200 m bl.sl and 3000 m bl.sl

The resistivity map at 200 m bl.sl (Figure 25, left) also outlines a conductive zone parallel and along the main faults in the area. This is probably due to the up flow of conductive geothermal waters through the fault zones and spreading out into the sediments along and above the fault zone (damage zones or fault splays).

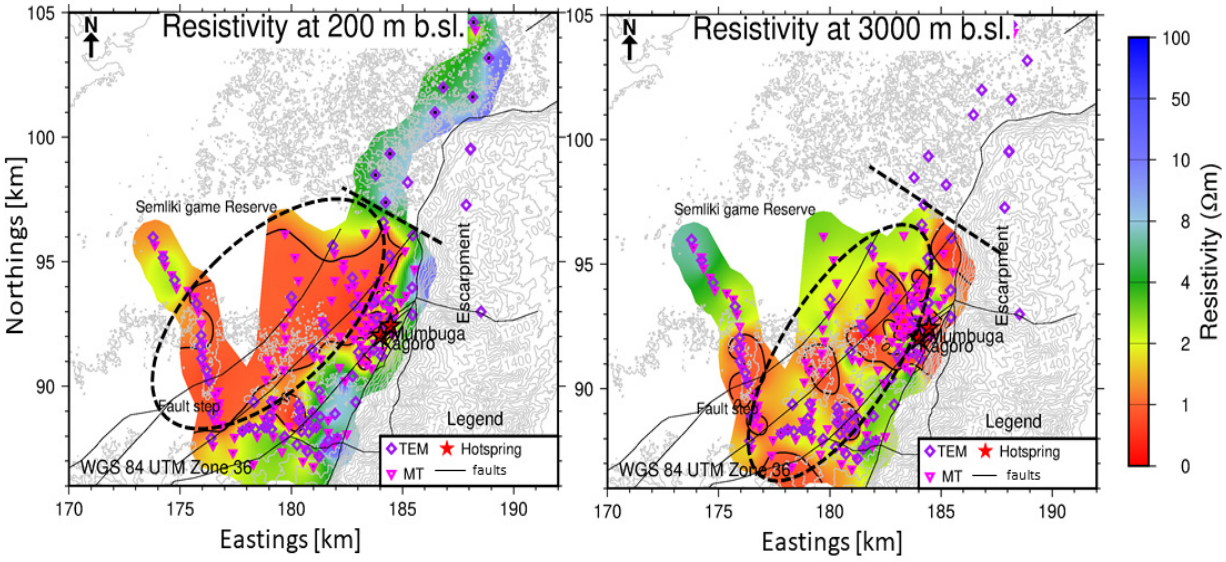

FIGURE 25: Resistivity depth slices at 200 m bl.sl (left) and 3000 m bl.sl. (right). Coordinates are in km

In the resistivity map, at 200 m bl.sl (about 900 m below surface, Figure 25 right), the conductive zone with a resistivity of 1-2 Ωm becomes very pronounced and clearly demarcated, starting near the hot spring area and spreading out towards the west indicating thick conductive which could be due to out-flow of the system into sediments. At this depth, the resistivity boundary in the NE and on the Eastern side is still maintained, clearly showing the high resistive Precambrian rocks of the mountain ranges and the conductive sedimentary basin in the graben.

Below 1200 m bl.sl the resistivity boundary towards the NE disappears. This is because this is below the depth of exploration the TEM soundings and the stations to the NE of the prospect are not used in the plotting of the resistivity map. Therefore, at greater depths, the TEM stations have been ignored. Other depths slices were produced and can be found in the appendix of this report.

At 3000 m b.s.l shown on the right in Figure 25, the area of the conductive zone starts to reduce towards the centre around the hot springs. There is a relatively resistive zone that starts to show up at greater depths probably indicating a gradual change from the conductive sediments into a more resistive unit at depth. The depth to basement at Buranga is not known, but a few kilometres north of the geothermal field, the bottom of the sediments was determined to be at 5000 m b.s.l using data from oil and gas wells.

5.3 Resistivity cross sections

A number of vertical resistivity cross sections were constructed as shown in Figure 26. The cross sections were generated using the TEMCROSS program which is a Linux based code developed at ISOR. Only few cross-sections will be discussed here (Figure 28 to Figure 34) but all 19 cross sections are made are available in the appendix to this report.

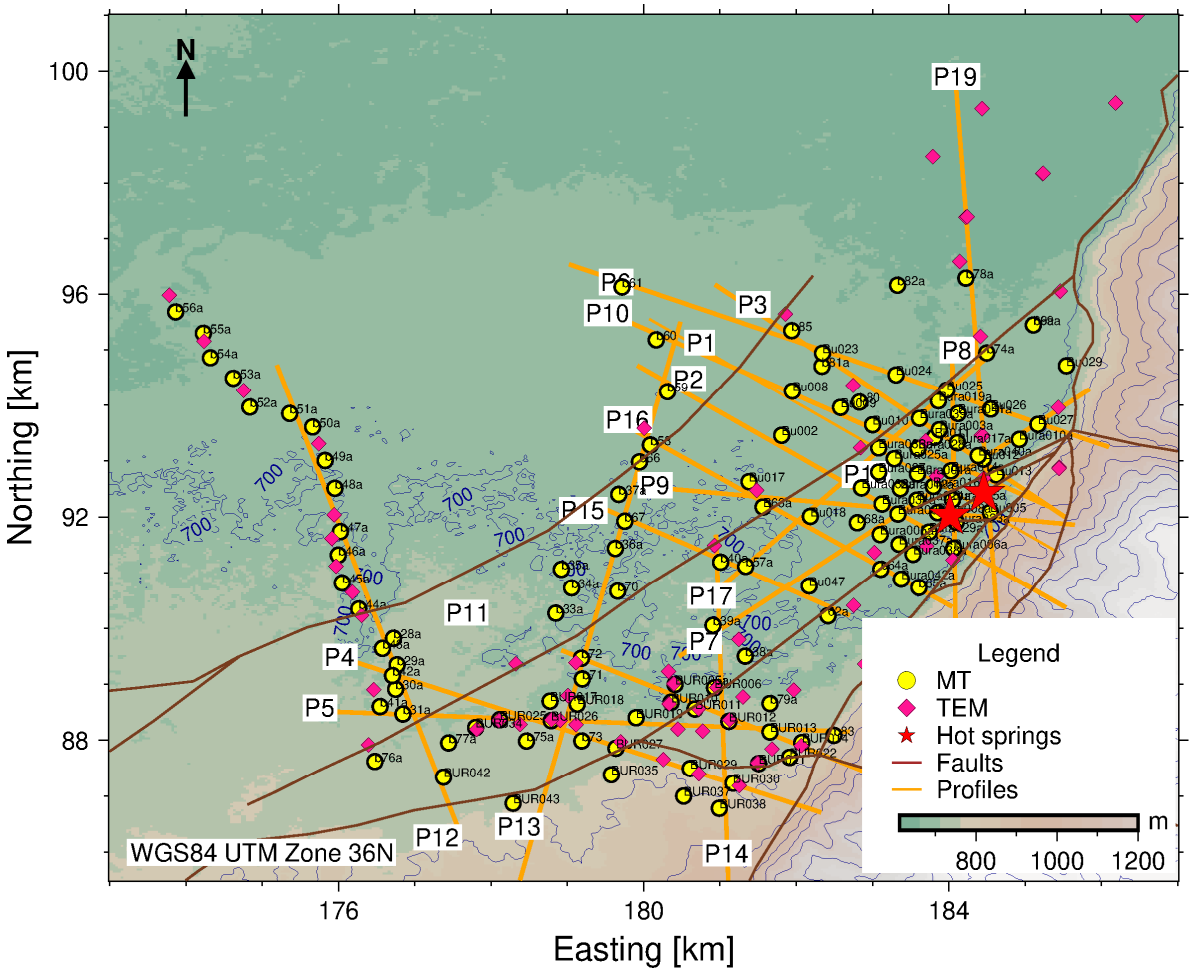

FIGURE 26: Location map showing profiles for resistivity cross sections

Profile 1

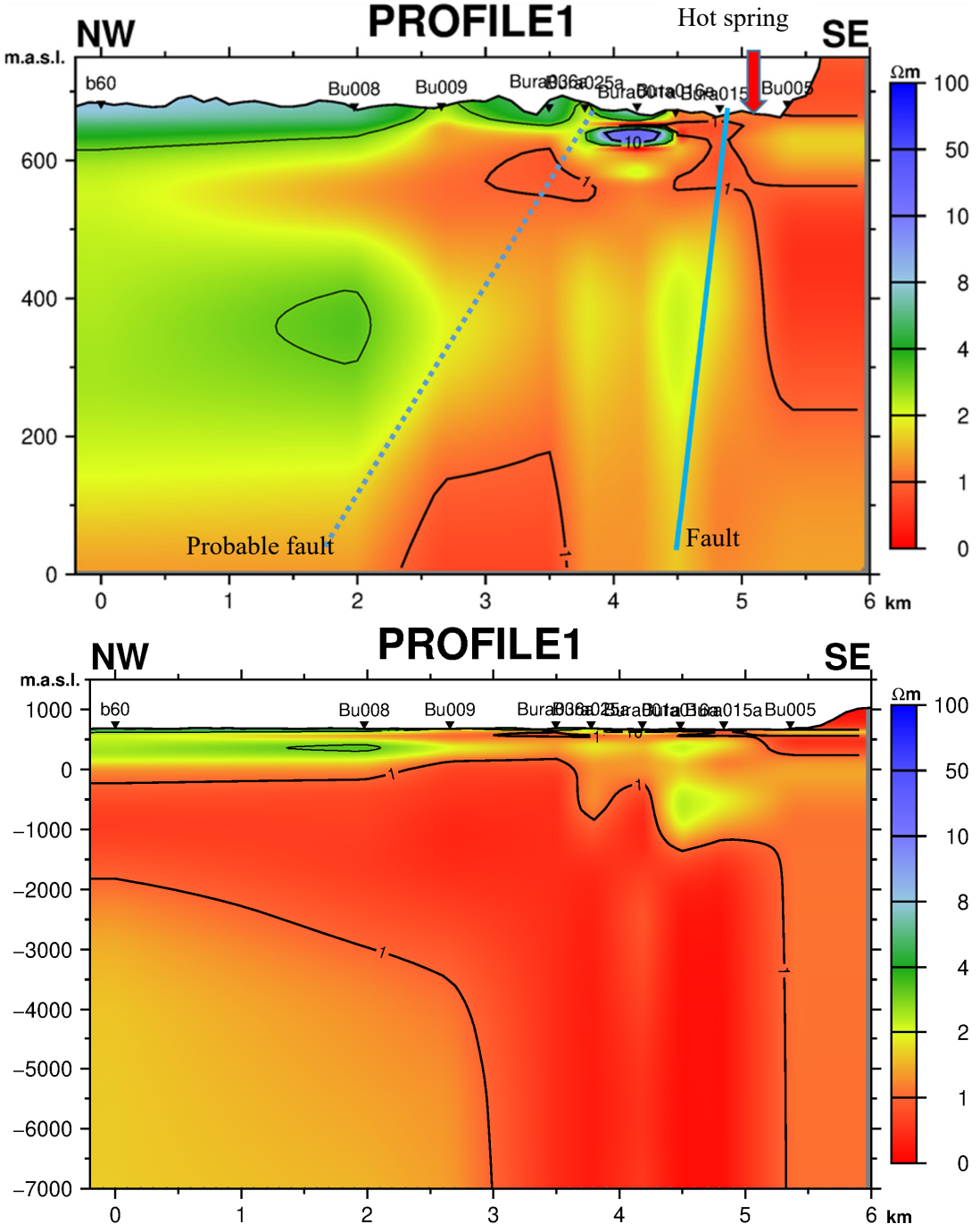

FIGURE 27: Resistivity cross section down to sea level (a) and down to 7000 m b.s.l (b)

Profile 1 (Figure 26 and 27) runs in NW-SE direction and passes near the Mumbuga hot spring area. Two sections reaching different depths were generated with one from the surface to sea level and the other from the surface down to 7 km b.s.l. The section shows a shallow less conductive region (structure) with a resistivity of about 1.4 - 3 Ωm at the centre of the section. On the deeper section to the right, the less conductive layer is seen to extend towards the SE and then becoming deeper, i.e. to depths of more than 3 km in the far SE. The more conductive parts of the section could probably be pointing at thick sedimentary layers (alluvial soils) that have filled up the graben over time.

Profile 2

Profile 2 (Figure 28 and 29) also runs in NW-SE direction through the prospect area and slightly intersects the southern part of the Kagoro hot springs. At shallow depths in the SE part of the profile, there is a very resistive Precambrian rock typical of the Rwenzori massif with a resistivity of >50 Ωm. In the NW part of the section, there is a 100 m thick layer with a resistivity of 3-7 Ωm overlying more conductive thick sedimentary layers that extend to depths of almost 4 km.

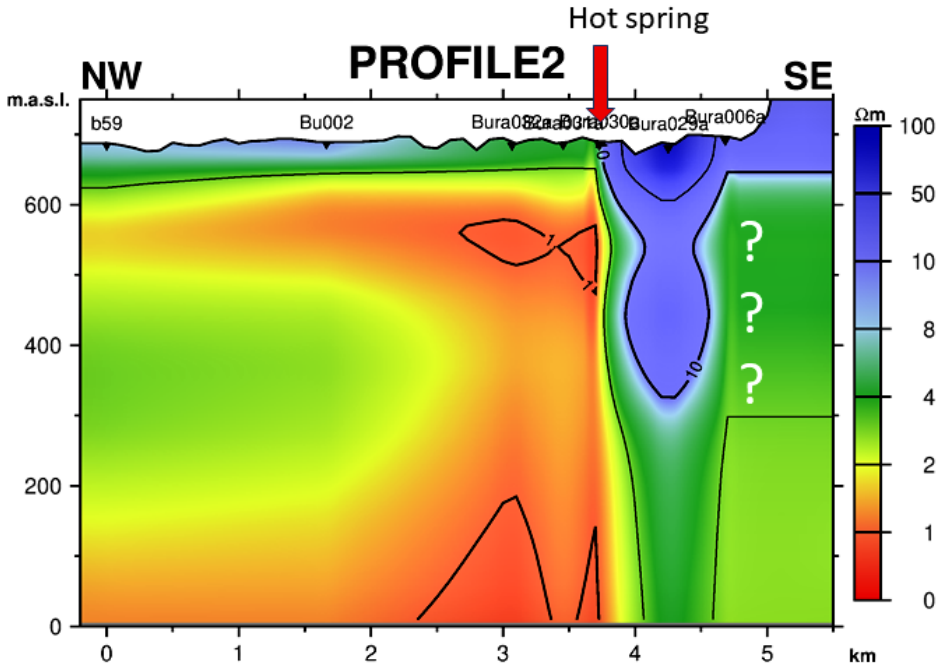

FIGURE 28: Resistivity cross section along profile 2. The question marks indicate an area of unreliable data from one station. The hot spring is located along the inferred fault

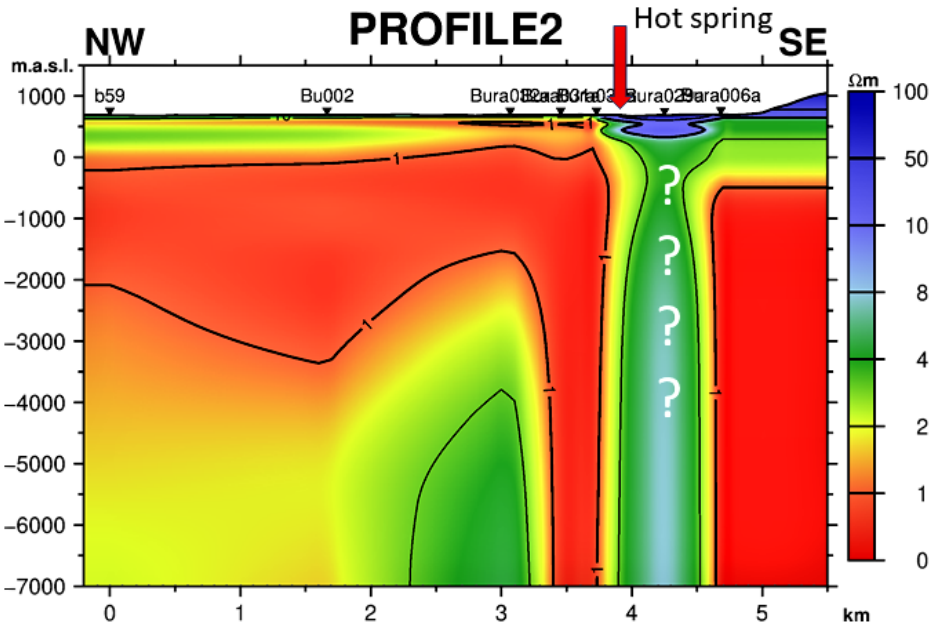

FIGURE 29: Resistivity cross section along profile 2 from surface down to 7000 m b.s.l. The question marks indicate an area of unreliable data from one station. The hot spring is located along the inferred fault

The model from station Bura029a stands out, probably due to bad/affected sounding data. This station alone cannot be relied on to give a conclusive resistivity structure since the inferred resistivity at that station is not confirmed by nearby stations as seen in Figure 31.

Profile 6 and 9

Profile 6 (Figure 30 and 31) is a NW-SE trending profile starting from the highly resistive Precambrian rocks of the host block in the SE at the near surface and towards the more conductive sediments to the NW. There is a low resistivity layer at about 700 m below the surface with a thickness of about 3 km at the most north-westerly side. This low restive cap is underlain by a relatively resistive layer from 4 km bl.sl.

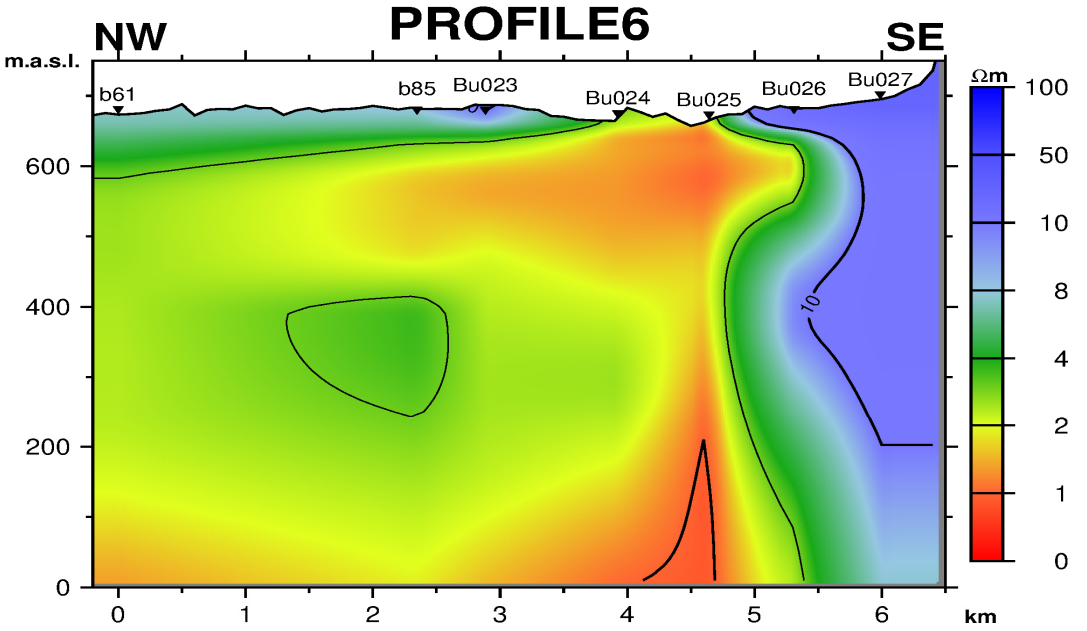

FIGURE 30: Resistivity cross section on profile 6 striking in NW-SE direction based on 1D joint inversion of MT and TEM data at Buranga at sea level

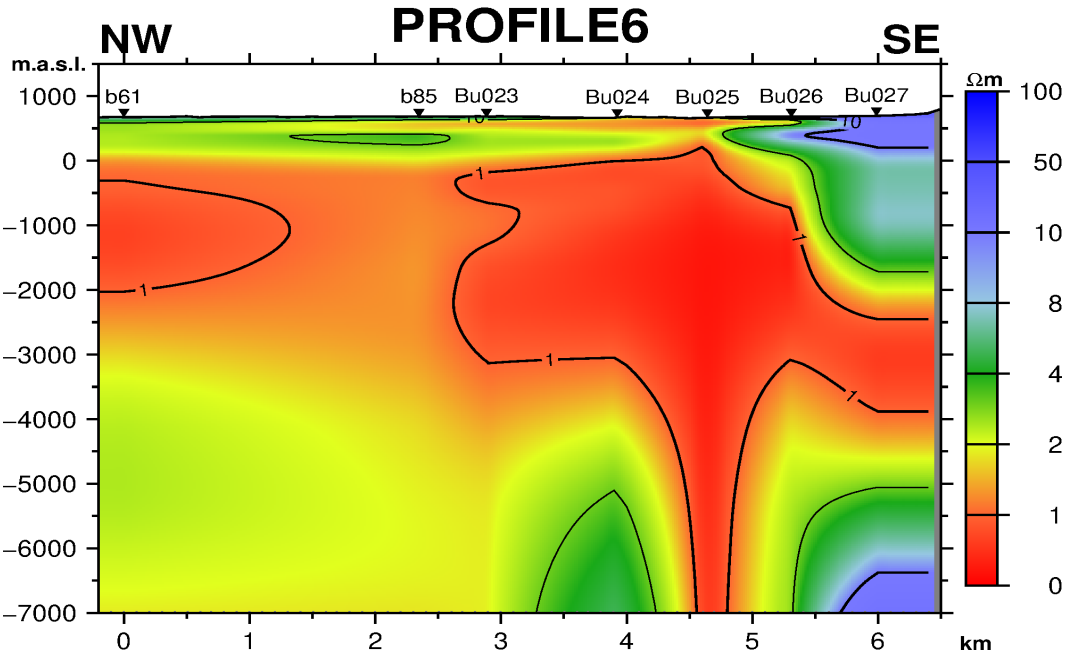

FIGURE 31: Resistivity cross section on profile 6 striking in NW-SE direction based on 1D joint inversion of MT and TEM data at Buranga down to 7 km

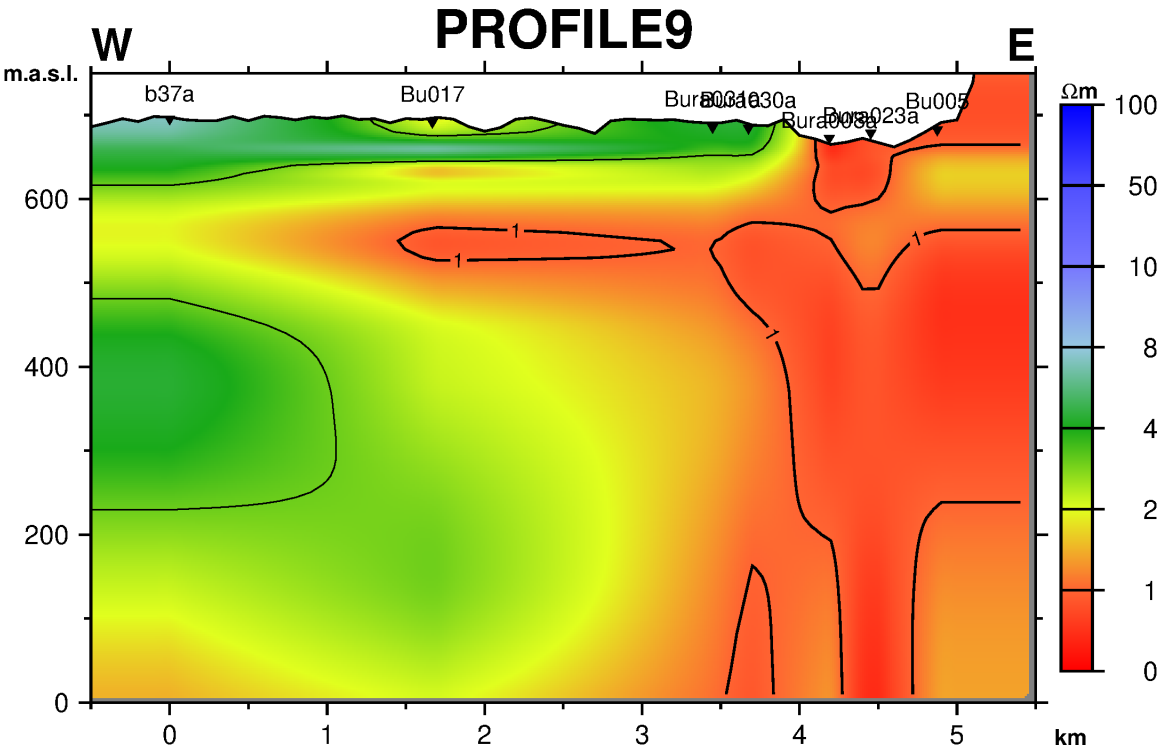

FIGURE 32: Resistivity cross section along profile 9 which is oriented in W-E direction down to sea level

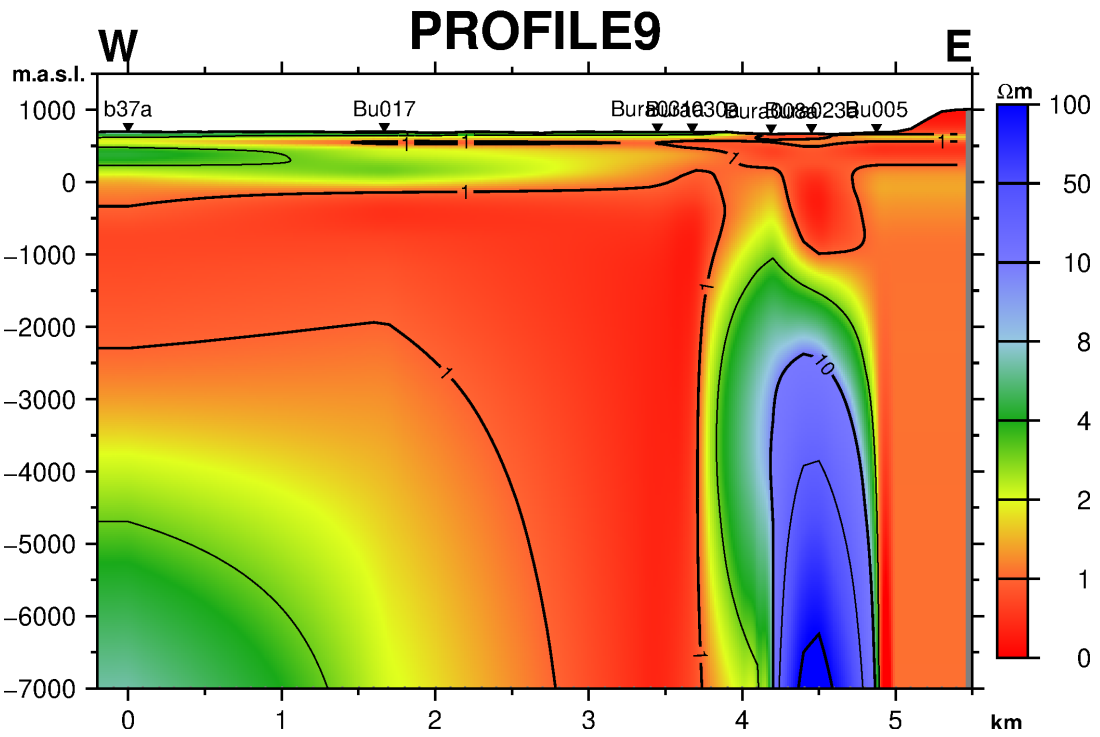

FIGURE 33: Resistivity cross section along profile 9 which is oriented in W-E direction down to 7,000 m b.s.l.

The profile (Figure 32 and 33) runs from the west to the east of the Buranga prospect crossing the Kagoro hot spring area and the faults inferred by geological mapping. The section shows a relatively resistive surface layer of about 2-5 Ωm which is 100 m thick from the western side towards the centre

and onto the far eastern end. At the centre, there is a more conductive layer extending to the surface creating a dome shape around a deep seated highly resistive body at 2 km below sea level. This resistive zone level could be an artifact due to poor-quality data since this structure cannot be seen in any of the other soundings. Data from this location should be re-acquired to eliminate any doubts.

Profile 19

Profile 19 (Figure 34) runs from the mid-southern part of the prospect to the northern side of the area at Buranga. This profile was constructed to investigate the resistivity boundary that was observed on the iso resistivity maps towards the north-eastern side of the survey area. In this section, the following can be observed:

(a) Indeed, there exists a clear resistivity boundary near station B78 where it is less resistive to the south and more resistive in the north. This resistivity boundary could represent a contact zone or a W-E cutting fault dipping to the north that is concealed by the vegetation in the area.

(b) The south of B78 is dominated by conductive alluvial soils (rift alluvium) or sediments with resistivity < 4 Ωm whereas northwards of B78 are probably the so-called mica schists and quarzitic interbeds with resistivity > 5 Ωm.

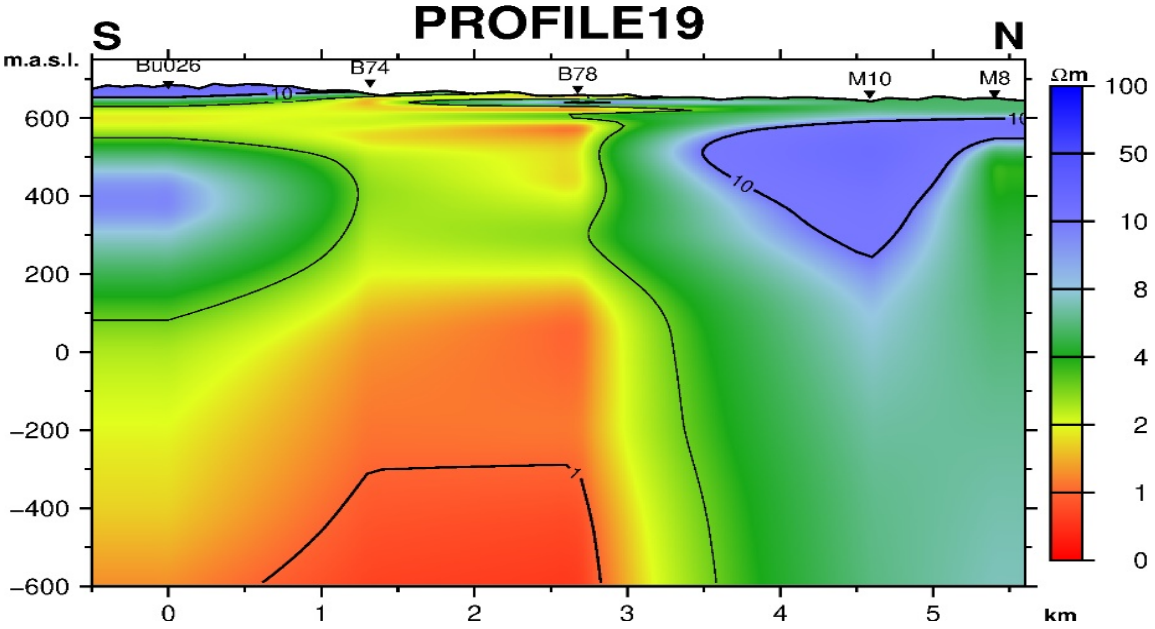

FIGURE 34: Resistivity cross section along profile 19 which is oriented in S-N direction based on 1D joint inversion of MT and TEM down to 600 m b.s.l

5.4 Geothermal significancy of results and Integrated interpretation

From the resistivity data and interpretation discussed above, the resistivity structure at Buranga can be described as follows:

(a) From near surface down to 400 m a.s.l.:

From the surface to a depth of about 200 m, the area is characterized by relatively resistive layers ranging from 8 Ωm on the westerly side to over 100 Ωm to the east towards the Rwenzori ranges. This corresponds to the relatively unaltered impermeable surface rocks to the east and to sedimentary/soil assemblages that have recently been deposited on the flood plain where there is constant deposition of surface soils from the Rwenzori.

(b) Below 400 m a.s.l to about 4 km b.s.l.:
There exists a thick conductive sedimentary layer(s) (approximately 4 km thick with resistivity <5 Ωm) near the hot spring area sand preading out in a near circular manner towards the west with the hot springs being located on its eastern margin. This low resistive layer could be due to up flow of geothermal fluids into the sediments towards the west.

(c) Below 4 km b.s.l.:
The thick conductive sediments extend to a depth of 4 km bl.sl. and are underlain by a relatively resistive layer of 4-8 Ωm in the western part. This indicates that the depth to the crystalline basement west of Buranga could be about 5 km. There is a clear contrast in the eastern most part with resistivities of > 50 Ωm. This is probably the basement rocks towards the Rwenzori. The resistivity boundary between the west and east at MT station Bu026 in cross section 19 could infer a deep-seated fault. This fault could be the pathway for deep circulating hot fluids to the hot springs at the surface above.

Geochemical and isotope hydrological studies by Ármannsson (1994) and Bahati et al. (2010) indicate that the fluids from the hot springs and hot pools at Nyansimbe and Kagoro are neutral with a PH of 7-8 and salinity of 14,000 – 17,000 mg/kg total dissolved solids. The conductivity of the fluids can explain the high conductivity (low resistivity) that is seen within the sediments. Geothermometry predicts subsurface temperatures of ~180°C and no indication of hydrogen was found in the gas analysis (Bahati et al., 2010) and there are no indications of mixing of the geothermal fluid with cold ground water.

6. CONCLUSION AND RECOMMENDATIONS

The Buranga geothermal prospect is a low temperature system with a distinct resistivity structure. The results presented here are consistent with the general view that the geothermal system is a deep circulation amagmatic system within tectonic faults, mining heat from the crustal heat flow. Up flow is mainly controlled by the major Bwamba bounding fault(s) which are permeable along their damage zones and fault splays which are directly associated with the N to NE striking west dipping faults as mapped by Hinz et al. (2018). Based on the distribution of active hot springs, the up flow is probably along multiple fault segments. The area has a very thick layer of sediments which are about 5 km deep in the central rift north of Buranga. The geothermal system has some outflow into these sediments and towards the western part of the prospect. Recharge is through meteoric water (Ármannsson, 1994, 2001) that runs from the Rwenzori ranges into the flood plain and then seeping through smaller fault terminations and displacement transfer zones that are present within this young faulting system.

No high resistivity core was detected at depth and no high temperature alteration detected. Estimated subsurface temperatures have been estimated slightly above 150°C. Smectite clays are the most probable alteration minerals to be expected in this area. The resistivity data in this study support previous ideas about Buranga geothermal system. The actual resistivity structure in the eastern part, in the vicinity of the controlling faults, is somewhat ambiguous due to poor data quality. Therefore, we recommend that higher quality resistivity data should be collected in the eastern part to better resolve the resistivity structure there.

A gravity survey should be undertaken on profiles running from Rwenzori into the sedimentary basin together with a local scale reflection/refraction seismic survey to map the topography of the basement. If such data exist from previous studies, they should be reviewed and used to constrain the current model.

When the current model has been improved by obtaining better quality resistivity data, gravity, and/or seismic data, then drilling of temperature gradient holes and/or an exploration well should be considered. Drilling of an exploration well should target the deep permeable fault zones which provide the up flow. Temperature gradient holes could help locating the up-flow fault(s) and define the extent of the geothermal system.

ACKNOWLEDGEMENTS

The six months training in Iceland has been an absolute eye opener in many aspects of my life but most importantly it has provided me with an opportunity to tap into the vast expertise and resources that the Icelandic Geosurvey (ISOR) has both in terms of human resource and industry-based technology. I would like to heartily thank my supervisors Mr. Knútur Árnason, Mr. Gylfi P. Hersir and Mrs. Ásdís, Benediktsdóttir for their guidance and stewardship during the lectures, data analysis and writing of my final project.

I also extend my sincere appreciation to the staff of the GROGTP, **Málfríður Ómarsdóttir**, **Ingimar G. Haraldsson**, **Vigdís Harðardóttir** and Director **Gudni Axelsson**, you went out of your way to see that all the fellows had a comfortable yet very in-depth learning experience. Continue doing good, like Mohamad Ali said, **"Doing good to others is the only rent we pay for our time on earth"**, I must tell you that you are premium customers in paying your rent on earth.

To my wife, kids, and entire family, I cannot thank you enough for all that you have continuously done for me while I was away. The encouragement and constant communication really kept me going and I really appreciate you all.

Finally, the GROGTP fellows, a new family away from home, I will always treasure the moments and interactions we have had and there is no doubt I would be happy to do this again with you all anytime.

REFERENCES

Ármannsson, H., 1994: *Geochemical Studies on Three Geothermal Areas in West and Southwest Uganda.* Geothermal Exploration -1 UGA/92/002 and UGA/92E01

Ármannsson, H., 2001: *Isotope geochemistry for geothermal resources exploration application to geothermal areas in Southwest Uganda.* Report on Expert Mission to Uganda for the IAEA Project UGA/8/003-02.

Árnason, K., 1989: *Central Loop Transient Electro-Magnetic Soundings Over a Horizontally Layered Earth*. OS-89032/JHD-06. Orkustofnun, National Energy Authority, Geothermal Division.

Árnason, K., 2006a: *TemX, short manual.* ÍSOR – Iceland GeoSurvey, Reykjavík, Iceland, internal report, 17 pp.

Árnason, K., 2006b: *TemX, a program for 1D inversion of central-loop TEM and MT data. Short manual*. ÍSOR – Iceland GeoSurvey, Reykjavík, Iceland, internal report, 17 pp.

Árnason, K., 2008: *The magnetotelluric static shift problem.* ÍSOR - Iceland GeoSurvey, Reykjavík, Iceland, report ÍSOR-08088, 16 pp.

Árnason, K., 2015: The static shift problem in MT soundings. *Proceedings of the World Geothermal Congress 2015, Melbourne, Australia,* 12 pp.

Bahati, G., Kato, V., and Nyakecho., C., 2010: Geochemistry of Katwe-Kikorongo, Buranga and Kibiro geothermal areas, Uganda. *Presented at the 3rd east African Rift geothermal conference (ARGEO-C3), Djibouti,* 6 pp.

Berdichevsky, M.N., and Dmitriev, V.I., 2008: Models and Methods of Magnetotellurics. *Springer*

Berlin Heidelberg, 125-126.

Bromley, C., 2018: The role of advanced geophysical monitoring in improved resource expansion and make-up drilling strategy. *Proceedings of the 43rd Workshop on Geothermal Reservoir Engineering, Stanford University, Stanford, California, SGP-TR-213,* 8 pp.

Caldwell, T.G., Bibby, H.M., and Brown, C., 2004: The magnetotelluric phase tensor. *Geophysical Journals International, 158,* 457–469.

Chave, D.A., Robe, L.E., Ian, J.F., Alan, G.J., Randall, L.M., William, L.R., Ari, V., and Peter, W., 2012: *Introduction to the magnetotelluric method.* Cambridge University Press, 14 pp.

Didas, M.M., 2018: 1D joint inversion of MT and TEM data from Ngozi geothermal prospect, SW-Tanzania – An integrated interpretation of geoscientific results. Report 13 in: *Geothermal Training in Iceland 2018.* UNU-GTP, Iceland, 141-185.

EAGER, 2017: Buranga and Panyimur review and conceptual models: *Unpublished Presentation to GRD, December 2017,* 76 slides.

EDICON, 1984: Aeromagnetic Interpretation of Lake Albert/Edward portion of the Western Rift Valley,*unpublished report* ,EDICON inc, Denver Colorado (1984).

Harris, N., Pallister, J.W., and Brown, J.M., 1956: Oil in Uganda. *Memoir No. IX, Geological Survey of Uganda*, 1-33.

Geotools, 2019: Magnetotelluric and Time Domain EM Data Analysis, User Guide.

Heath, J., Sussman, D., Lonsdale, A., and Bayarsaikhan, M., 2018: Advancing geothermal development in East Africa: lessons learned during the 2015-2018 EAGER programme. *Proceedings of the 7th African Rift Geothermal Conference 2018, Kigali, Rwanda,* 13 pp.

Hersir, G.P., and Árnason, K., 2013: Resistivity of rocks. *Presented at Short Course VIII on Exploration for Geothermal Resources, organized by UNU-GTP, GDC and KenGen, Lake Bogoria and Lake Naivasha, Kenya,* 8 pp.

Hersir, G.P., Gudnason, E.Á., and Flóvenz, Ó.G., 2021: Geophysical exploration techniques. In: Letcher, T., (ed.), *Comprehensive Renewable Energy – 2nd edition, Vol 7*. Elsevier, Oxford – in press.

Hinz, N., Cumming, B., and Sussman, D., 2018. Exploration of fault-related deep-circulation geothermal resources in the western branch of the East African Rift System: Examples from Uganda and Tanzania. *Proceedings of the 7th African Rift Geothermal Conference 2018*, Kigali, Rwanda.

Jones, A.G., and Groom, R.W., 1993: Strike-angle determination from the magnetotelluric impedance tensor in the presence of noise and local distortion: rotate at your peril. *Geophysical J. International, 113(2),* 524-534.

Kahwa, E., 2012: Geophysical exploration of high-temperature geothermal areas using resistivity methods – case study: Theistareykir area, NE-Iceland. Report 14 in*: Geothermal Training in Iceland 2012.* UNU-GTP, Iceland, 235-263.

Kahwa, E., Nishijima, J., and Fujimitsu, Y., 2020: Subsurface characterization of Panyimur geothermal prospect, NW Uganda using magnetotelluric data. *Proceedings of the 8th African Rift Geothermal Conference Nairobi, Kenya,* 11 pp.

Kato, V., 2017: Geothermal exploration in Uganda, status report. *Presented at SDG Short Course II on Exploration and Development of Geothermal Resources, organized by UNU-GTP, GDC and KenGen, Lake Bogoria and Lake Naivasha, Kenya,* 24 pp.

Vozoff, K., 1972: The Magnetotelluric Method in the Exploration of Sedimentary Basins. *Geophysics, 37*, 98-141.

Lindenfeld, M., Rumpker, G., Batte, A., and Schumann, A., 2012*:* Seismicity from February 2006 to September 2007 at the Rwenzori Mountains, East African Rift: earthquake distribution, magnitudes and source mechanisms. *Solid Earth, 3,* 251-264.

McConnell, R.B. and Brown, J.M., 1954: *Drilling for geothermal power at Buranga hot springs, Toro*. Geological Survey of Uganda, unpublished report R.B.M/16.

Morley, C.K., and Westcott, W.A., 1999: Sedimentary environments and geometry of sedimentary bodies determined from subsurface studies in East Africa. In: Morley, C.K., (ed.), *Geoscience of Rift Systems-Evolution of East Africa*. AAPG Studies in Geology 44, 211 - 231.

Natukunda, J.F., 2010: Geology of Kibiro, Katwe and Buranga geothermal prospects of Uganda. *Proceedings of the World Geothermal Congress 2010, Bali, Indonesia,* 11 pp.

Nyaketcho, C., 2008: Preliminary environmental impact assessment for the development of Buranga geothermal prospect, Uganda. Report 26 in: *Geothermal Training in Iceland 2008.* UNU-GTP, Iceland, 447-476.

Ochmann, N., Lindenfeld, M., Barbirye, P., and Stadtler, C., 2007: Microearthquake survey at the Buranga geothermal prospect, Western Uganda. *Proceedings of the Thirty-Second Workshop on Geothermal Reservoir Engineering, Stanford University, Stanford, United States,* 8 pp.

Phoenix geophysics, 2018: MTU-5C User manual.